ORIGINAL PAPER

Phase-Field Simulation of Hydraulic Fracturing by CO_2 and Water with Consideration of Thermoporoelasticity

Yixuan Feng[1] · Abbas Firoozabadi[1]

Abstract

We have advanced phase-field simulation of hydraulic fracturing with consideration of thermoporoelasticity and discretization based on the mixed finite element in temperature, pressure, and the phase field. The key application is intended for hydraulic fracturing by water and by CO_2 in hot dry rock. In geothermal fracturing, the injection fluid may have much lower temperature than the hot-volcanic rock and consideration of thermoporoelasticity may have a significant effect. We provide numerical simulations and comparison with laboratory data and examine the effect of thermoporoelasticity on breakdown pressure and fracture intensity. The thermal effect is more pronounced under unconfined conditions, especially for CO_2 fracturing. The change of granite rock strength in the Brazilian tests at different temperatures without specific fluid confinement may not apply to high stress boundary conditions. Based on simulation of hydraulic fracturing experiments using water in heated and unheated granite, we conclude that the critical energy release rate G_c which is a key parameter of the phase field is not affected by temperature in the range of 20–300 °C. In that respect, there is similarity on the independency of Young's modulus from temperature. The critical stress is, however, known to be a function of temperature. An important observation relates to simulation of fracturing by water and CO_2 in a domain larger than laboratory scale. CO_2 fills the created fractures quickly. Filling of created fractures by water takes time, and as a result fractures propagate in many stages. We observe from simulations that fracture intensity from CO_2 is higher than by water in line with laboratory measurements. Higher fracture intensity and fracture surface area is an important consideration in renewable energy production from geothermal formations due to low thermal conductivity in volcanic rocks.

Highlights

- The phase-field model predicts a single long fracture by water in granite at low temperature, and vast fracture network at geothermal conditions.
- The phase-field predicts, in line with experiments, lower breakdown pressure and higher fracture density by CO_2 than by water.
- Phase-field simulation of geothermal formulations is advanced to capture extensive branching observed in laboratory scale.
- The critical energy release rate G_c of granite-water may not be affected by temperature in the range of 20–300 °C.
- In large scale, fracturing by water may go through a cycle of stop and go, while continuous CO_2 fracture propagation is more likely.

✉ Abbas Firoozabadi
abbas.firoozabadi@Rice.edu

1 Department of Chemical and Biomolecular Engineering, Rice University, Houston, TX, USA

List of Symbols

B	Bulk modulus
c	Phase-field variable
C_f	Compressibility of the *fluid*
C_{Pf}	Heat capacity of fluid at constant pressure per *unit mass*

$C_{V,s}$	Heat capacity of solid at constant strain per *unit mass*
E	Young's modulus
f	Local load applied on the external boundary
G_c	Critical energy release rate
H	Strain-history field
k_R	Permeability of *rock*
l_0	Regularization length
M	Biot's modulus
p	Fluid pressure
Q_p	Volumetric *injection rate*
T	Temperature
t	Time
$\ddot{\mathbf{u}}$	Acceleration
$\mathbf{x}$	Location coordinate
$\alpha_{T,f}$	Coefficient of thermal *expansion of fluid*
$\alpha_{T,s}$	Coefficient of linear thermal expansion of *the solid rock*
ϕ	Porosity of rock
μ	*Fluid viscosity*
ν	Poisson's ratio
α	Biot's coefficient
ρ_f	*Fluid density*
ρ_s	Mass density of the solid rock
λ_f	Fluid thermal *conductivity*
λ_s	Solid thermal *conductivity*
ε	Strain tensor
ε_{vol}	Volumetric strain
ψ_e	Elastic strain energy density of the strain tensor
χ_R, χ_F	Linear indicator functions of phase-field variable

1 Introduction

Geothermal formations in the subsurface have generally higher temperature than oil and gas formations at the same depth. These formations often consist of volcanic rocks of low permeability and low connected porosity and low thermal conductivity. The energy content of the rock can potentially be a source of renewable energy production. When the rock contains steam and it can flow to the surface, electricity can be generated from expansion of steam in a turbine. When the rock is hot, but the permeability and porosity is low, a heat carrier fluid can be injected and produced. To access the rock energy, a large surface area would be required; the heat carrier fluid will pick up heat and deliver it at surface for electricity generation. CO_2 may be a fluid of choice (Bongole et al. 2019; Brown 2000; Pruess 2006). One major difference between fracturing geothermal formations and tight hydrocarbon formations is the effect of high rock temperature on fracturing by colder fracturing fluid. The effect of thermoporoelasticity on fracturing is potentially large. In a recent paper, we have discussed a major difference between CO_2 and water fracturing; CO_2 results in

lower breakdown pressure and higher fracture density than water (Feng et al. 2021). Majority of publications report lower fracturing pressure by CO_2 compared to water. There are limited experiments which report the opposite (Al Shafloot et al. 2021; Li et al. 2016). In the experiments by Al Shafloot et al. (2021), the injection rate in CO_2 fracturing (2 mL/min) is 20 times of water fracturing (0.1 mL/min). In the experiments by Xiang Li et al. (2016), the injection rate in CO_2 fracturing (5 mL/min) is 5 times of water fracturing (1 mL /min). In addition, condensation is observed by Xiang Li et al. (2016) which is not considered in current work. Higher injection rate generally leads to higher breakdown pressure (Feng et al. 2021), but there may be other mechanisms at play that lead one to conclude breakdown pressure by CO_2 may be higher than by water in shale formations. Based on molecular simulations, we calculate much lower critical energy release rate, G_c, for CO_2-kerogen than H_2O-kerogen (Wu and Firoozabadi 2022). G_c is a key parameter in fracturing of rocks; lower G_c implies lower fracturing pressure and higher fracture intensity. We have simulated the CO_2 fracturing experiments by Al Shafloot et al. (2021). CO_2 reaches the outer boundary within 500 s which is much earlier than the breakdown time of around 3000 s in experiments. We therefore conclude that the change of effective stress at the outer boundary is possibly the reason for apparent high breakdown pressure for CO_2. Details of simulation are presented in Supporting Information S1.

This work centers on investigation on effect of thermoporoelasticity in fracturing of volcanic rocks and the numerical simulation of the process by CO_2 and water fracturing fluids. There are reports in the literature showing that in CO_2 fracturing of rock with the same initial temperature as the injected CO_2, there may be a change in temperature of CO_2 (Inui et al. 2014; Ishida et al. 2012; Kizaki et al. 2012). The change in temperature is more likely from compression and expansion. In enhanced geothermal systems, the injection of cold fluid into hot formation leads to large temperature changes and thermal stress can play a significant effect (Chen and Zhou 2021, 2022; Ghassemi and Zhou 2011; Stephens and Voight 1982; Tao and Ghassemi 2010; Tarasovs and Ghassemi 2012; Zhang et al. 2021). The thermoporoelasticity may have a large effect on fracture initiation and fracture propagation. In the following, we will first review the experimental work in the literature on the effect of thermoporoelasticity and fluid type on fracturing. Then review of simulation of fracturing will be followed.

1.1 Laboratory Experiments

1.1.1 Thermal Effect from Fluid Expansion

Temperature change has been observed in laboratory experiments on CO_2 fracturing of rock with about the same initial

temperature as the injected fluid. Ishida et al. (2012) have conducted hydraulic fracturing experiments on Kurokami-jima granite using liquid and supercritical CO_2. The temperature of fluid in the injection hole is measured. For both liquid and supercritical CO_2, the temperature remains nearly constant in the pressure buildup stage, and a drop of temperature (from 40 to 30 °C for supercritical CO_2, and from 16 to 0 °C for liquid CO_2) is observed at the breakdown pressure. The authors suggest the temperature drop is due to adiabatic expansion of CO_2 by flow through the created fractures. The same group (Inui et al. 2014) later have conducted hydraulic fracturing experiments on the same samples with water, oil, and supercritical CO_2. A temperature change is measured in CO_2 fracturing. Extended fractures and branching are observed in CO_2 fracturing. As expected, no temperature change is observed in injection of water and the oil. Kizaki et al. (2012) compare CO_2 fracturing with water fracturing in Inada granite and Ogino tuff. During pressure buildup, the temperature increases by 2 °C for granite and 6 °C for tuff due to adiabatic compression of CO_2. After the breakdown, the temperature decreases due to adiabatic expansion of CO_2. No significant change of temperature is observed for water fracturing. More fracture branches are observed for CO_2 in granite than by water. The authors reason higher fracture density and lower breakdown pressure is due to lower viscosity of CO_2. These suggestions do not consider the fluid-rock energy density (Wu and Firoozabadi 2021, 2022). In the experiments by Ishida et al. (2004), the breakdown pressure is 16.5 MPa for viscous oil and 17.9 MPa for water. The results are not consistent with viscosity reasoning. The viscosity of oil is 80 folds greater than that of water (Ishida et al. 2012). As stated, surface energy of fluid-rock may be the main reason for difference in fracture density.

1.1.2 Thermal Effect from Temperature Difference

The thermal effect is the likely main difference between fracturing of enhanced geothermal systems (EGS) and shale reservoirs. Kumari et al. (2018) report the results from injection of 20 °C water into Harcourt granite in the temperature range of 20–300 °C with confining pressures. With an increase in confining pressure, the breakdown pressure increases. With an increase in rock temperature, the breakdown pressure drops. More fractures around notch are observed at higher temperature difference between injected fluid and rock. Zhou et al. (2018) inject 20 °C water into granite from 20 to 400 °C. The breakdown pressure drops with the increase in temperature, and more transverse fractures are observed at high temperature. Zhou et al. (2018) reason that the thermal tensile stress around the borehole induced by rapid cooling of the rock has a more significant effect on breakdown pressure, than the change in rock

mechanical parameters. They show that tensile strength of granite only has a 2.2% drop (1.1 MPa) from 100 to 450 °C, while the breakdown pressure decreases by 67.9% (32.4 MPa) from 100 to 400 °C. Zhang et al. (2021) inject 32 °C distilled water into granite at three temperatures of 50, 100, and 200 °C, with and without boundary loads. The breakdown pressure is lower at higher temperature without boundary loads. Most of the studies so far have focused on water fracturing and pressure–time history. To the best of our knowledge, there are few laboratory experiments of CO_2 fracturing on enhanced geothermal systems at high temperatures. Isaka et al. (2019) have conducted CO_2 fracturing on Harcourt granite samples with the same size as in Kumari et al. (2018). The temperature of granite is varied from 50 to 300 °C, and CO_2 at the injection point has 10–220 °C lower temperature than granite. The effects of confining pressure and rock temperature on breakdown pressure are consistent in water fracturing. CO_2-induced fractures are more tortuous than water-induced fractures and have more branching under high temperature. Pramudyo et al. (2021) have conducted similar experiments as Isaka et al. (2019) by injecting room temperature CO_2 into Inada granite from 200 to 450 °C. Complex cloud-fracture networks are observed. The fracture network is formed from pre-existing microfractures instead of the borehole.

1.2 Numerical Simulations

1.2.1 Thermal Effect from Fluid Expansion

The temperature of CO_2 changes from expansion and compression. There is limited literature on numerical simulations of thermal effect from fluid expansion in fractures. Li et al. (2018) simulate the fluid expansion from one fracture to another fracture. There is no fracture propagation in this work. The fluid expands from one fracture at a high pressure of 60 MPa to the other fracture with low pressure of 30 MPa. Both fractures have the same initial temperature of 110 °C. The temperature of CO_2 increases in the second fracture to 140 °C and decreases in the first fracture to as low as 80 °C. In another example with water, there is no appreciable temperature change.

1.2.2 Thermal Effect from Temperature Difference

Zhang et al. (2021) have conducted numerical simulations of thermal effect on fracturing using damage evolution law in COMSOL. Simulation results for pressure–time history agree with experiments. Very small fluctuations in measured pressure profiles are reproduced, which may indicate extensive parameter adjustment. CO_2 fracturing is also simulated and compared with water fracturing. More branches in water fracturing are observed away from the well location.

The authors reason the observation to be due to higher heat capacity of water. Higher fracture density from CO_2 is simulated in the near-well zone. Zhang et al. (2021) explain that the fracture extending capacity is poor due to CO_2 low viscosity. There is no significant difference in the overall simulated fracture density from water and CO_2. Guo et al. (2020) have simulated water fracturing in 2D by damage evolution law in COMSOL. The temperature of water fracturing fluid is 20 °C and the rock is 200 °C. A single fracture is simulated. Sensitivity analysis is conducted, and the authors conclude that higher Young's modulus would lead to lower breakdown pressure and longer fractures. Both lower heat capacity of the rock and higher initial temperature difference would lead to larger temperature change in rock. Higher Young's modulus leads to larger bulk modulus for a constant Poisson's ratio. Higher temperature drop, higher bulk modulus, and higher thermal expansion coefficient all lead to higher tensile thermal stress. Increased rock heterogeneity results in weaker planes in rock, so the fracture initiation pressure is lower, and propagation becomes faster as well. Salimzadeh et al. (2018) have simulated injection of 20–83 °C CO_2 into 83 °C reservoir with faults in field scale for CO_2 storage. Fracture propagation only occurs when CO_2 is below 40 °C. Alpak (2021) has recently simulated hydraulic fracturing with thermal effect. He uses a discrete approach of cohesive-zone method. The critical energy release rate G_c is used to determine the critical fracture width. The value of G_c is not reported. The simulations are conducted by injection of 75 °F water, 150 °F water, and 140 °F CO_2 into 150 °F formation. For water fracturing, the non-isothermal condition results in a longer fracture and a wider width. CO_2-induced fractures have much smaller length and width than water-induced fractures due to higher leak-off, as the simulated deepwater reservoir has a much higher permeability (as high as 1100 md) and porosity (0.26–0.325) than volcanic rocks. The author assumes the fracture propagation to be confined within a planar predefined surface. Thermal effect on fracture pattern is not discussed. Another recent work on simulation of geothermal fractured formations is by Zheng et al. (2021). The focus of the work is application of the extended embedded discrete approach with unstructured triangular elements in fractures and structured Cartesian elements in matrix rock. The method follows the conventional stress and effective stress formulation. Effect of natural fractures on the creation of new hydraulic fractures is investigated.

A comparison of CO_2 and water hydraulic fracturing has been made by Bongole et al. (2019). The initial state is defined by a large number of natural fractures. A conventional fracturing model is used in the investigation based on the Coulomb failure expression. The major parameters of the model are the principal stresses, friction angle, Coulombic cohesive force, and calibration parameters. In the energy balance, the heat exchange between the fracture and matrix is based on convection coefficient. The equations describing the problem are numerically solved by the Galerkian method for pressure, displacement, and temperature using COMSOL. Numerical results show that the heat recovery by CO_2 is significantly higher than by water. There is also a report of isothermal hydraulic fracturing of granite at room temperature and high temperature by water (Liu et al. 2022) both isothermally. Therefore in their work, there is no need for thermoelasticity. Liu et al. use the damage zone model with spatial discretization by the conventional finite elements. Natural fractures are introduced in the simulations.

1.3 Phase-Field Model

The phase field is perhaps the method of choice to simulate fracture initiation and complex fracture geometry and propagation (Chen et al. 2022, 2020; Sun et al. 2021). The method has been extended to include thermoelasticity (Blaise Bourdin et al. 2014; Miehe et al. 2015; Rahbar et al. 2021; Tangella et al. 2021) and more recently to include thermoporoelasticity (Li et al. 2021; Noii and Wick 2019). In geothermal hydraulic fracturing, the consideration of thermoporoelasticity in the phase-field step is a key. Noii and Wick present a comprehensive work in relation to hydraulic fracturing in geothermal formations. In their formulation, there are a number of assumptions including the effect of temperature on fluid pressure to be negligible. The authors use the Galerkian finite element in the discretization of pressure, temperature, displacement, and phase-field variables. They have verified their algorithm with analytical solutions. The critical energy release rate, G_c, which is a key parameter in the phase field is assumed to be about of 10^5 N/m. As a result of high critical energy rate, the numerical results reveal simple fractures. The recent work by P. Li et al. (2021) accounts for the effect of temperature on fluid properties but assumes a small constant compressibility for CO_2 to allow linearization. In the discretization, the Galerkian method is used in COMSOL. The authors use $G_c = 1.05 \times 10^3$ N/m. There is no observation of fracture branching in the numerical results.

Despite much progress in numerical solution of fracturing in EGS systems, the validation of the phase field based on laboratory data is not yet reported. The discretization using the mixed finite element for pressure and temperature may have merits over the Galerkin method (Feng et al. 2021). For laboratory-scale experiments and perhaps in field scale, we may need to include the effect of kinetic term which is not included in the literature work on thermoporoelasticity. In the phase field, the lower critical energy release rate, G_c, for CO_2 compared to water may lead to lower breakdown pressure and more branching in CO_2 fracturing than in water (Feng et al. 2021). Despite the fact that a large number of authors suggest lower fluid viscosity may lead

to fracture branching, our recent work is not in support of viscosity effect alone (Feng et al. 2021). Viscosity of water drops significantly at high temperature (water viscosity is only about 3.4 times of CO_2 at 300 °C). The viscosity difference between water and CO_2 becomes less significant in geothermal formations at high temperature. The breakdown pressure is based on rock material properties in both the damage evolution law and cohesive-zone numerical methods. In the damage evolution law, the stress condition of rock is compared to the maximum tensile or shear stress criterion. In the cohesive-zone method, the critical fracture opening displacement is determined based on linear elastic fracture mechanics. The effect of fluid is considered only through pressure. In phase-field simulations, the critical energy release rate, G_c, is used which is related to the solid–fluid interfacial energy density (Wu and Firoozabadi 2021, 2022); the effect of fluid–rock interaction is therefore a key parameter in our work.

1.4 Fracture Filling

In domain sizes larger than 1-to-2-inch cores, when boundary load is low, fracturing may take place multiple times before the created fractures reach the boundary. If the fluid pressure drops significantly at the first breakdown and the domain is sufficiently large, subsequent pressure buildup stages are needed for pressure increase from injection for further fracturing. In the experiments of Zhou et al. (2018), consecutive pressure buildup of seven times is observed in water fracturing. The first fracturing has the highest breakdown pressure. The created fracture is partly empty, and a liquid because of low compressibility cannot fill the created space. Injection will be required to fill the created space and build up the pressure. According to laboratory experiment observation by Daneshy (1978), fracture tip is always ahead of fracturing fluid which fills 60–70% of created fracture. Even fluids in the tight rock around the fractures may not fill the created space rapidly. In overburdened reservoirs, the fluid lag may not be likely (Detournay 2016). We will discuss the issue of fracture filling in some detail as part of this work.

In the following, we will first present the phase-field formulation in hydraulic fracturing with consideration of thermoporoelasticity. The numerical solution of the four set of differential equations is then discussed. In the past, we have verified our hydraulic fracturing code with the analytical work of fracturing by Sneddon and Lowengrub (1969) at isothermal conditions. In this work, we will further verify the fracture creation and propagation at isothermal conditions.

Our numerical simulations are also, compared with analytical solution (Li et al. 1998) in deformable hot rock when it is exposed to a cold fluid in a suddenly cooled wellbore. Next, we simulate the experiments in water and CO_2 fracturing from laboratory measurements by Kizaki et al. (2012), Watanabe et al. (2017), Kumari et al. (2018), and Isaka et al. (2019). We also simulate fracture initiation and propagation in a domain 5 times of the size of the laboratory experiments to gain insight into fluid filling of the created fractures and creation and propagation of new fractures from continuous fluid injection.

2 Theory

2.1 Governing Equations

In this work, we add the contribution from thermal effect to various balances that define the problem at isothermal conditions. First, we add the contribution from thermal effect in the momentum balance expression. We also add the contribution of thermal effect in the mass balance expression and add the energy balance equation. The momentum balance of a deformable rock is given by

$$\frac{\partial \left[(1-c)^2 \frac{\partial \psi_e^+}{\partial \epsilon_{ij}} + \frac{\partial \psi_e^-}{\partial \epsilon_{ij}} \right]}{\partial x_j} - \alpha_{eff} \frac{\partial p}{\partial x_j} - 3B\alpha_{T,s} \frac{\partial T}{\partial x_j} + f_j = \rho_s \ddot{u}_j \quad j = 1, 2, \tag{1}$$

where c is the phase-field variable; x is the location coordinate; ϵ is the strain; p is the pressure of fluid; f is the local load applied on the external boundary; $\ddot{u}$ is acceleration; ψ_e^+ and ψ_e^- are the elastic strain energy density of positive and negative components of the strain tensor, respectively;

$\alpha_{eff} = \chi_R \alpha + \chi_F$ is the effective Biot's coefficient, and the linear indicator functions are given by $\chi_R = (c_2 - c)/(c_2 - c_1)$, $\chi_F = (c - c_1)/(c_2 - c_1)$, where c_1 and c_2 are the two threshold values. We use c_1 and c_2 from Lee et al. (2016); B is the bulk modulus; $\alpha_{T,s}$ is the coefficient of linear thermal expansion of the solid rock; T is the temperature; ρ_s is the mass density of the solid rock; i is a dummy index; and j is a free index.

The phase-field equation is given by

$$2(1-c)H - G_c \frac{c}{2l_0} + 2l_0 G_c \frac{\partial^2 c}{\partial x_i^2} = 0, \tag{2}$$

where G_c is the critical energy release rate, l_0 is the regularization length, and the H is strain-history field. Details are presented in the Supporting Information S1 (Borden et al.

2012; B. Bourdin et al. 2000; Francfort and Marigo 1998; Gershenfeld 1998; Griffith 1921; Miehe et al. 2010; S. Zhou et al. 2019).

The fluid mass balance is expressed as

$$
\rho_f \frac{1}{M} \frac{\partial p}{\partial t} + \rho_f \alpha_{eff} \chi_R \frac{\partial \varepsilon_{vol}}{\partial t}
$$
$$
+ \rho_f \big(3\chi_R \phi_{eff} \alpha_{T,s} - \phi_{eff} \alpha_{T,f} - 3\chi_R \alpha_{eff} \alpha_{T,s}\big)\frac{\partial T}{\partial t} \qquad (3)
$$
$$
- \rho_f \frac{k_{eff}}{\mu}\nabla^2 p - \frac{k_{eff}}{\mu}\nabla \cdot \big[\rho_f \big(C_f \nabla p - \alpha_{T,f}\nabla T\big)\big] = Q_p,
$$

where t is the time, $k_{eff} = \chi_R k_R + \chi_F k_F$ is effective permeability of the rock, the fracture permeability $k_F = \frac{w^2}{12}$, w is the width of the fracture, μ is fluid viscosity, ρ_f is fluid density, Q_p is the volumetric injection rate, ε_{vol} is the volumetric strain, $\alpha_{T,f}$ is the coefficient of thermal expansion of fluid, the effective porosity $\phi_{eff} = \chi_R \phi + \chi_F$, C_f is the compressibility of the fluid, and M is the Biot's modulus. The effective properties $(\alpha_{eff}, k_{eff}, \phi_{eff})$ are used to describe the transition region (Lee et al. 2016; Zhou et al. 2019). In our previous work (Feng et al. 2021), fracture is fixed after creation. In this work, we update the fracture width w and therefore it may change.

The energy balance is expressed as

$$
\big(\phi_{eff}\rho_f C_{P,f} + \big(1 - \phi_{eff}\big)\rho_s C_{V,s}\big)\frac{\partial T}{\partial t}
$$
$$
- \phi_{eff}\rho_f C_{P,f}\frac{k_{eff}}{\mu}\nabla p \cdot \nabla T + 3\big(1 - \phi_{eff}\big)B\alpha_{T,s}T\frac{\partial \varepsilon_{vol}}{\partial t}
$$
$$
= \big(\phi_{eff}\lambda_f + \big(1 - \phi_{eff}\big)\lambda_s\big)\nabla^2 T \qquad (4)
$$
$$
+ \phi_{eff}\alpha_{T,f}T\bigg(-\frac{k_{eff}}{\mu}\nabla p \cdot \nabla p + \frac{\partial p}{\partial t}\bigg),
$$

where $C_{P,f}$ is the heat capacity of fluid at constant pressure per unit mass, $C_{V,s}$ is the heat capacity of solid at constant strain per unit mass (Smejkal et al. 2021), λ_s is the solid thermal conductivity, and λ_f is fluid thermal conductivity. Details of energy balance formulation are presented in Text S7 of the Supporting Information S1 (Bird et al. 2002).

2.2 Discretization of the Governing Equations

The displacement, phase-field, fluid pressure, and temperature are solved from Eqs. (1), (2), (3), and (4), respectively; a staggered scheme is used in the numerical solution. We use the finite element for the discretization of the displacement in Eq. 1, and the mixed finite element for the discretization of the phase-field variable c in Eq. 2, pressure in Eq. 3,

and temperature in Eq. 4. The mixed hybrid finite element in our simulations allows accurate calculations in fractured media and results in conservation of energy and mass as well as direct calculation of mass leak-off between the fracture and the matrix. It also allows direction calculation of energy transfer between the fractures and the matrix. The merits in accurate calculations of flow are presented in Text S8 of the Supporting Information SI (Chavent and Roberts 1991; Hoteit and Firoozabadi 2004; Zidane and Firoozabadi 2014).

For element K, the matrix notation of Eq. (1) after discretization is given by

$$
\mathbf{KD}_K - \mathbf{Q}_1\mathbf{P}_K - \mathbf{Q}_2\mathbf{T}_K + \mathbf{M}\ddot{\mathbf{D}}_K = \mathbf{F}, \qquad (5)
$$

where $\mathbf{D}_K$, $\mathbf{P}_K$, $\mathbf{T}_K$, and $\ddot{\mathbf{D}}_K$ are the matrices for displacement, pressure, temperature, and acceleration fields, respectively; $\mathbf{F}$ is the external forces at the nodes; $\mathbf{K}$ is the stiffness matrix; $\mathbf{Q}_1$ is the poroelasticity matrix; $\mathbf{Q}_2$ is the thermoelasticity matrix; and $\mathbf{M}$ is the mass matrix, bold fonts indicate vector or matrix. Details are presented in the Supporting Information S1 (Kleiven et al. 2001; Zienkiewicz 1982).

Equation (2) after discretization becomes

$$
2\big(1 - c_K\big)H - G_c\frac{c_K}{2l_0} + \frac{2l_0 G_c}{a}\sum\big(A_K^{-1}\big(c_K^n DIV_K - TC_K\big)\big) = 0, \quad (6)
$$

where a is the area of the element, $DIV_K = [1, 1, 1]^T$ for a triangular element, c_K is the element average of phase-field variable, TC_K is the average phase-field variable on different edges of element K, and A_K is related to basis function with details in Text S8 of the Supporting Information SI.

Equation (3) from time and spatial discretization becomes

$$
\rho_f \frac{1}{M}\frac{p_K^n - p_K^{n-1}}{\Delta t} + \rho_f \alpha_{eff}\chi_R \frac{\varepsilon_{vol}^n - \varepsilon_{vol}^{n-1}}{\Delta t}
$$
$$
+ \rho_f\big(3\chi_R\phi_{eff}\alpha_{T,s} - \phi_{eff}\alpha_{T,f} - 3\chi_R\alpha_{eff}\alpha_{T,s}\big)\frac{T_K^n - T_K^{n-1}}{\Delta t}
$$
$$
+ \frac{\rho_f}{a}\frac{k_{eff}}{\mu_f}\sum\big(A_K^{-1}\big(p_K^n DIV_K - TP_K\big)\big)
$$
$$
- \frac{k_{eff}}{\mu}\nabla p \cdot \big[\rho_f\big(C_f\nabla p - \alpha_{T,f}\nabla T\big)\big] = Q_p,
$$
$$
(7)
$$

where superscript n and $n - 1$ indicates current and previous times, Δt is the time interval between the steps, and T_K is the element average of temperature. Newton's backward difference is used for time discretization.

Equation (4) from time and spatial discretization becomes

$$
\begin{aligned}
&\left(\phi_{eff}\rho_f C_{P,f} + \left(1-\phi_{eff}\right)\rho_s C_{V,s}\right)\frac{T_K{}^n - T_K{}^{n-1}}{\Delta t} \\
&- \phi_{eff}\rho_f C_{P,f}\frac{k_{eff}}{\mu}\nabla p\cdot\nabla T + 3\left(1-\phi_{eff}\right) \\
&B\alpha_{T,s}T_K{}^n\frac{\varepsilon_{vol}{}^n - \varepsilon_{vol}{}^{n-1}}{\Delta t} = \frac{\phi_{eff}\lambda_f + \left(1-\phi_{eff}\right)\lambda_s}{a} \\
&\sum\left(A_K^{-1}\left(T_K{}^n \boldsymbol{DIV}_K - \boldsymbol{TT}_K\right)\right) \\
&+ \phi_{eff}\alpha_{T,f}T_K{}^n\left(-\frac{k_{eff}}{\mu}\nabla p\cdot\nabla p + \frac{p_K{}^n - p_K{}^{n-1}}{\Delta t}\right)
\end{aligned}
\tag{8}
$$

where $\boldsymbol{TT}_K$ is the average temperature on different edges of element K.

Details are presented in Text S8 of the Supporting Information SI (Chavent and Roberts 1991; Hoteit and Firoozabadi 2004; Zidane and Firoozabadi 2014).

3 Numerical Simulations

The focus of our work is 2D unstructured discretization of equations describing hydraulic fracturing with consideration of thermoporoelasticity. Unstructured triangle elements are used in all examples. In this work, when we refer to element size, it is based on the average side length of a triangular element. We assume single phase flow. At high temperature, the pressure of water is assumed to remain above saturation pressure, and CO_2 remains at supercritical state. The density and compressibility of CO_2 are calculated based on the Peng-Robinson equation of state (Peng and Robinson 1976). The viscosity of CO_2 is calculated from the Lohrenz-Bray-Clark model (Lohrenz et al. 1964). The thermal conductivity, heat capacity of CO_2, and temperature-dependent material properties of water are calculated from the empirical equations (Castro et al. 1986; Eckert 1987; Poling et al. 2001; Reid 1975). Young's modulus and Poisson's ratio of granite are assumed to be constant in the temperature range studied according to measurements of Isaka et al. (2018).

Our numerical simulations are first compared with analytical solution (Li et al. 1998) in deformable hot rock when it is exposed to a cold fluid in a suddenly cooled wellbore. We also further verify our model in fracture propagation and geometry at isothermal conditions. We next simulate the experiments in water and CO_2 fracturing from laboratory measurements by Kizaki et al. (2012). The fluid and rock have the same initial temperature. Temperature change in CO_2 fracturing is examined. The simulations of laboratory experiments by Watanabe et al. (2017) and Kumari et al. (2018) on water fracturing, and Isaka et al. (2019) on CO_2 fracturing of enhanced geothermal systems are also presented. Fracture initiation and propagation are examined as well as thermal effects. We also simulate

fracturing in a domain 5 times of the size of the laboratory experiments to gain insight into fluid filling in the created fractures and creation and propagation of new fractures due to continuous fluid injection. Dry rock is assumed (not saturated with fracturing fluid) as the initial condition unless specified otherwise. We use a time step size of about 1 s during pressure buildup before fracturing and small time-step size (about 1 μs) during fracture propagation.

We have verified fracture propagation at isothermal conditions. The verification is beyond what we presented in Feng et al. (2021). We simulate fracturing by water in a cement rock with natural fracture of different orientations in full predictions and compare the simulations with observed fracturing in different experiments. There is good agreement. Results are presented in Text S9 of the Supplementary Information.

3.1 Simulation of Hot Rock with Suddenly Cooled Wellbore and Comparison with Analytical Solution

We verify the coupled hydro-thermal–mechanical model with an analytical solution for hot rock with suddenly cooled wellbore (Li et al. 1998). The setup is the same as the numerical simulation by Ghassemi and Zhang (2004). An infinite-acting rock domain is assumed in analytical solution. In our simulations, the saturated rock is 2 m in diameter with a 0.2 m-diameter borehole at the center, as shown in Fig. 1a. Closed boundary condition is assumed for pressure domain, and insulation boundary condition is assumed for temperature. Free boundary condition is assumed for displacement. The initial temperature is 200 °C and the initial pressure is zero. The wellbore wall is suddenly cooled and maintained at 80 °C. The relevant parameters are listed in Table 1. The analytical solution of temperature, pressure, tangential stress, and radial stress distributions at 10^2, 10^3, 10^4, 10^5, 10^6 s are presented in Ghassemi and Zhang (2004). We only compare solutions at 10^2, 10^3, and 10^4 s since the boundary effect is significant at later times.

Figure 1b shows the temperature distributions over time from borehole wall to the outer boundary. Heat conduction is the dominant effect, and the rock temperature drops gradually starting from the borehole wall as illustrated in Fig. 1c–e. Figure 1f shows the pressure profile. A pressure drop is observed around borehole at the beginning due to the thermal contraction of rock from cooling. The pressure change is much faster than temperature change as expcted (see Fig. 1g–i). The simulation results are in good agreement with the analytical solution.

Figure 2a shows the tangential stress distributions over time from borehole wall to the outer boundary. The shrinkage of the rock near borehole due to cooling induces tensile stress. Figure 2b shows the radial stress profile. The shrinkage of the rock near borehole pulls the outer layer which

Fig. 1 a Geometry, and the analytical solution and our numerical results (Ghassemi and Zhang 2004); **b** temperature plot; **c–e** temperature profiles at different times; **f** pressure plot; and **g–i** pressure profiles at different times. $R = 1$ m
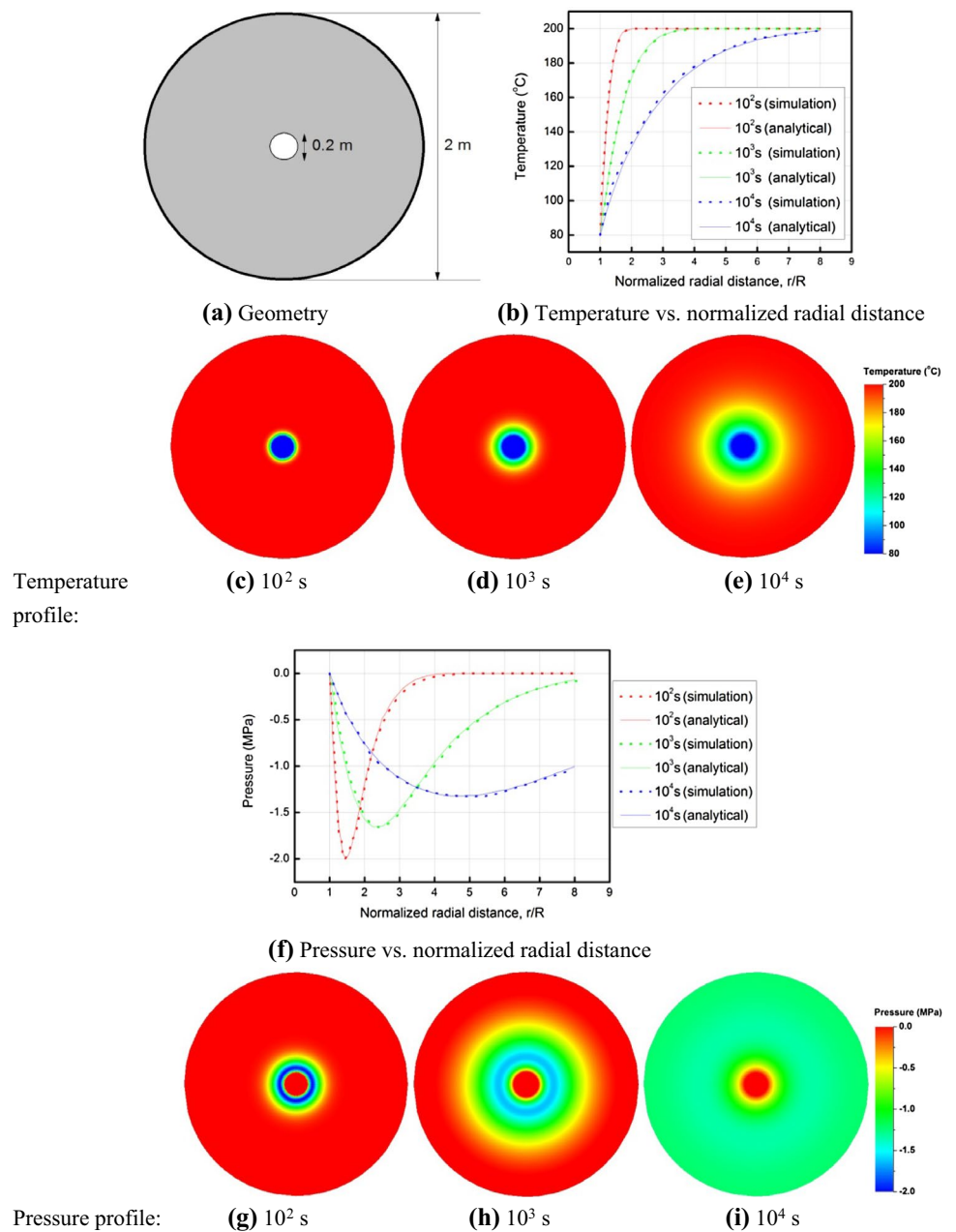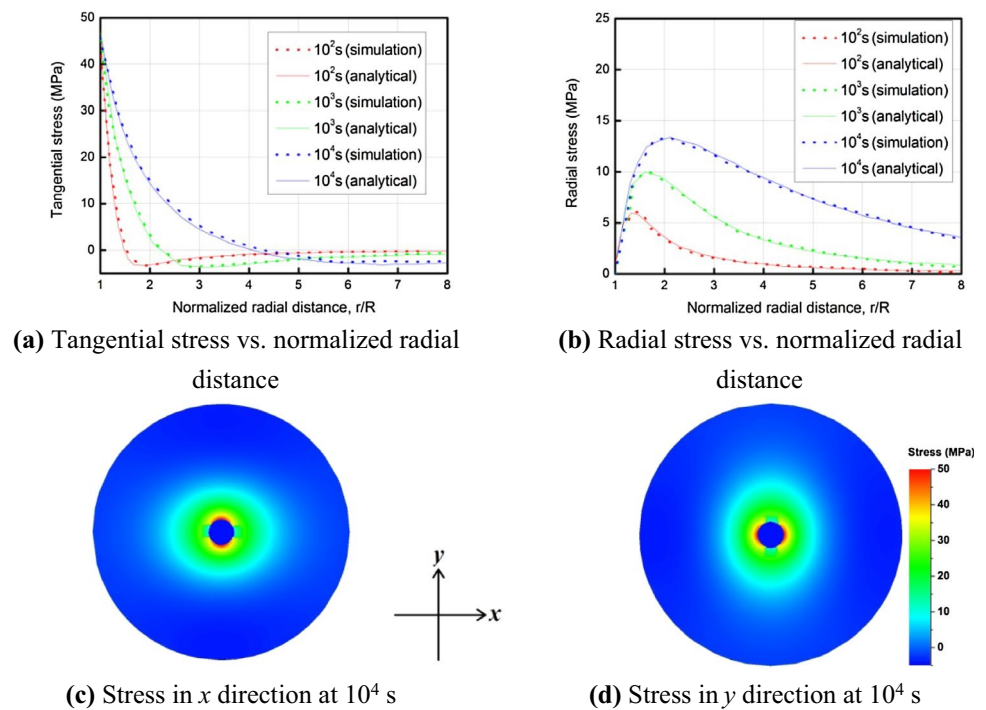

(a) Geometry

(b) Temperature vs. normalized radial distance

Temperature profile:

(c) 10^2 s   **(d)** 10^3 s   **(e)** 10^4 s

(f) Pressure vs. normalized radial distance

Pressure profile: **(g)** 10^2 s   **(h)** 10^3 s   **(i)** 10^4 s

Table 1 Parameters of analytical solution (Ghassemi and Zhang 2004) (α is obtained based on Skempton's coefficient; C_f is obtained based on bulk modulus; λ_f and λ_s are obtained based on heat capacity and thermal diffusivity)

E	3.75×10^7 Pa	ν	0.25	$\alpha_{T,s}$	2.4×10^{-5} K^{-1}
$\alpha_{T,f}$	3×10^{-4} K^{-1}	C_{Pf}	790 J/(kg K)	$C_{V,s}$	790 J/(kg K)
ϕ	0.01	ρ_f	1000 kg/m^3	α	0.443
k_R	4.053×10^{-4} mD	C_f	4×10^{-7} Pa^{-1}	Element size	1 cm
μ	3.55×10^{-4} Pa·s	λ_f	49 W/(m K)	λ_s	11.08 W/(m K)

induces a tensile stress. Figure 2c, d shows the stress profile at 10^4 s. Cartesian coordinate system is used in stress calculation. Stress in the direction along the *x* axis gives the radial stress, while along the *y* axis gives the tangential stress. The simulation results are in good agreement with the analytical solution.

Fig. 2 **a** Tangential stress plot; **b** radial stress plot; **c** profiles of stress in the *x* direction at 10^4 s; and **d** profiles of stress in the *y* direction at 10^4 s. $R = 1$ m

(a) Tangential stress vs. normalized radial distance

(b) Radial stress vs. normalized radial distance

(c) Stress in *x* direction at 10^4 s

(d) Stress in *y* direction at 10^4 s

3.2 Hydraulic Fracturing by Water and by CO_2: Unheated Inada Granite

Kizaki et al. (2012) have conducted laboratory-scale experiments in fracturing of cubic Inada granite rocks. Water is used to fracture an unheated dry granite. CO_2 fracturing is also conducted in unheated granite. The measurements on fracture breakdown pressure and fracture geometry provide a unique opportunity for analysis and to obtain the critical energy release rate of H_2O-Inada granite and CO_2-Inada granite. The core geometry is shown in Fig. 3a. The sample is 150-mm cube. The notch has a diameter of 20 mm. Triaxial loading is applied in the experiments with a vertical stress of 1 MPa and two horizontal stresses σ_H (5 MPa) and σ_h (3 MPa). Only horizontal stresses are considered in our 2D simulations. The roller boundary condition is applied on remaining edges, with one corner fixed. The boundary is closed with no flow in the experimental setup. Two simulations are conducted for fracturing: one for water and one for CO_2. The relevant parameters are listed in Table 2. Q_p is based on injection rate (50 mL/min) and length of hole (60 mm) from the experiments by Kizaki et al. (2012). Specimens for CO_2 fracturing are heated to 40 °C, and the temperature of specimens for water fracturing is 9 °C. Water has the same initial temperature as the rocks. It takes 22 s before water fills the notch and pressure starts to increase in experiment. The simulation also starts at 22 s to match the experiment condition. For CO_2 fracturing, liquid CO_2 is injected in the experiment and then heated to supercritical

state. The pressure is kept constant until 120 s, at which the simulation starts. We assume that the Inada granite is saturated at 120 s to compensate for the leak-off in first 120 s.

Figure 3b, c shows pressure vs. time in the notch. The pressurization rate is lower for CO_2 due to high compressibility. The breakdown pressure is lower in CO_2 fracturing. Figure 3d shows temperature vs. time in the notch in CO_2 fracturing. In simulations, the temperature of CO_2 increases slightly during pressure buildup due to compression, as shown in Fig. 3e. The temperature change correlates with the pressurization rate, which is the highest at 120 s, and the corresponding temperature is the highest at 41.2 °C. After the breakdown, the temperature of CO_2 in the notch drops rapidly due to expansion and increases in fractures because the fluid flows in and pressure increases, as shown in Fig. 3f. The temperature change is more significant after breakdown, since both the depressurization rate in the notch and pressurization rate in the fracture are much higher than the rate during pressure buildup. The water- and CO_2-induced fracture patterns are illustrated in Fig. 3g, h, respectively. A bi-wing fracture is observed for water fracturing, and the CO_2-induced fracture has branching. Our simulated results are in good agreement with the experimental data. Based on the simulations, we obtain the critical energy release rate for water-Inada granite ($G_c = 35$ N/m) and CO_2-Inada granite ($G_c = 25$ N/m). There has been no report of the critical energy release of granite with water and other fluids. Note that there is not a significant difference between the critical energy release rates of the two fluids with the Inada granite.
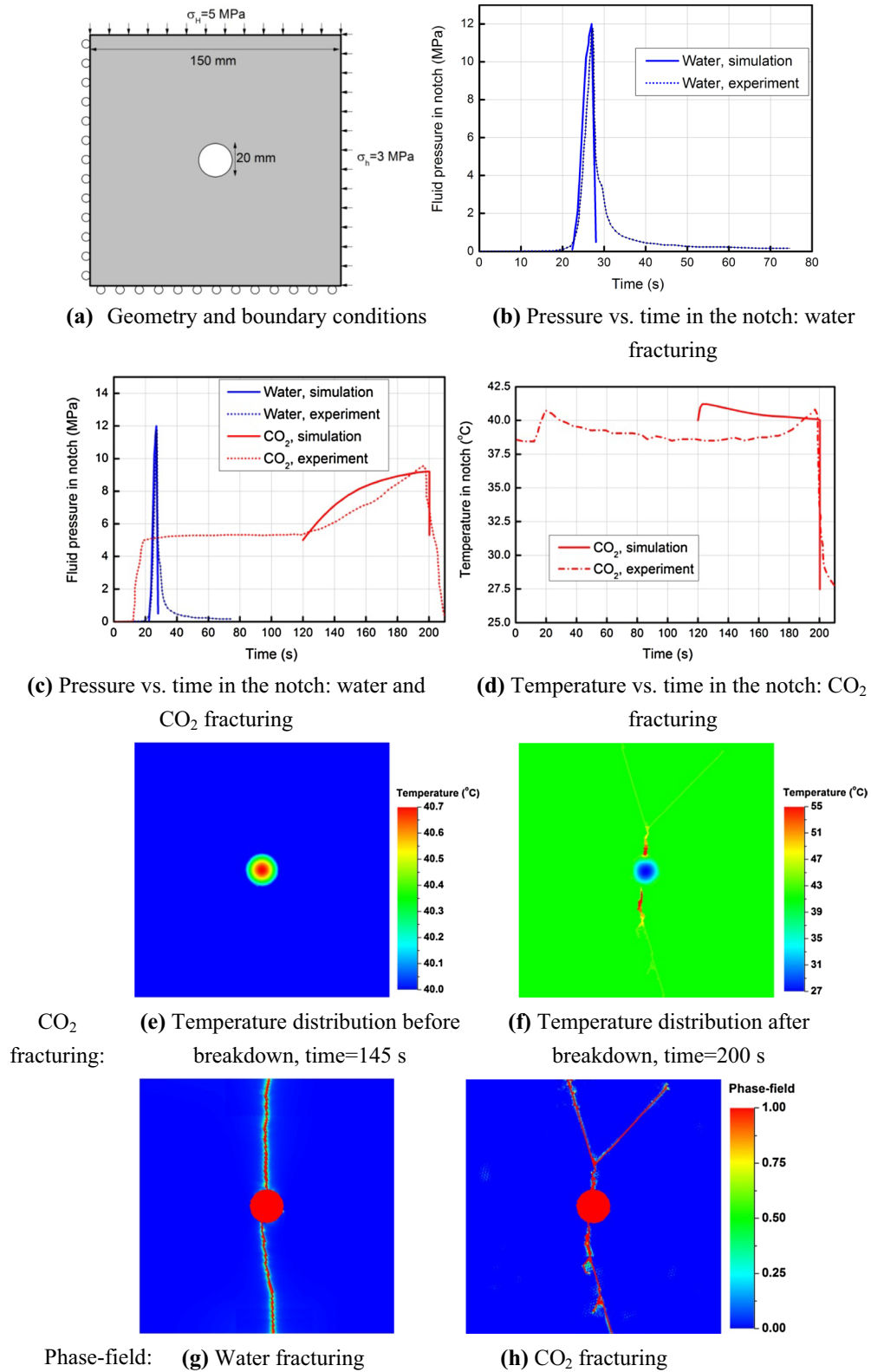
(a) Geometry and boundary conditions

(b) Pressure vs. time in the notch: water fracturing

(c) Pressure vs. time in the notch: water and CO_2 fracturing

(d) Temperature vs. time in the notch: CO_2 fracturing

CO_2 fracturing:

(e) Temperature distribution before breakdown, time=145 s

(f) Temperature distribution after breakdown, time=200 s

Phase-field:

(g) Water fracturing

(h) CO_2 fracturing

Fig. 3 **a** Geometry and boundary conditions of the setup from Kizaki et al. (2012); **b, c** pressure, and **d** temperature in the notch vs. time in water and CO_2 fracturing; simulated temperature distributions **e** before breakdown and **f** after breakdown in CO_2 fracturing; phase field in **g** water, and **h** CO_2 fracturing

Table 2 Relevant parameters in simulation of experiments by Kizaki et al. (2012) (G_c is obtained by matching the breakdown pressure; material properties of Inada granite are from Lin (2002))

E	6.21×10^{10} Pa	ν	0.3	$\alpha_{T,s}$	2.4×10^{-5} K^{-1}
$\alpha_{T,f}$	3×10^{-4} K^{-1}(water) 4×10^{-3} K^{-1}(CO$_2$)	$C_{P,f}$ (water)	4200 J/(kg K)	$C_{V,s}$	790 J/(kg K)
ϕ	0.0075	ρ_f (water)	1000 kg/m^3	α	0.0075
k_R	4.053×10^{-4} mD	C_f (water)	4.6×10^{-10} Pa^{-1}	G_c	25 N/m (CO$_2$-Inada granite) 35 N/m (water-Inada granite)
μ (water)	1.3×10^{-3} Pa s	λ_f (water)	0.6 W/(m K)	λ_s	11.08 W/(m K)
l_0	1 mm	c_1	0.4	c_2	0.6
Element size	0.5 mm	Q_p	14 mm^2/s		

In shale rock, the difference is very significant (Feng et al. 2021).

3.3 Hydraulic Fracturing by Water: Heated Inada Granite

Watanabe et al. (2017) have conducted experiments in water fracturing of small cores of Inada granite. The experiments are conducted in unheated Inada granite without confining pressure, and with confining pressure of 40 MPa at 200 °C and 360 °C. The injected water is preheated to the prescribed temperature before it enters the sample, so there are no initial temperature differences. An axial pressure of 90 MPa is also applied in the experiments, which is not considered in our 2D simulations. The geometry is shown in Fig. 4a. The cylindrical sample is 30 mm diameter and length of 25 mm. The notch has a diameter of 1.5 mm. The sample is wrapped with the polyimide film. Closed boundary condition with no flow is applied for pressure in line with experimental setup. The relevant parameters of our simulations are listed in Table 3. Q_p in 2D is based on injection rate (3 mL/min) and length of hole (10 mm) from the experiments.

We conduct simulations in isothermal condition in line with experimental setup, and in nonisothermal condition assuming water is injected at 20 °C and not preheated. Figure 4b–d shows pressure vs. time in the notch. The difference between measured and simulated breakdown pressure is less than 8% for the three conditions. The breakdown pressure is higher than the confining pressure. When there is a temperature difference between rock and fluid, a thermal tensile stress is induced around the notch which lowers the breakdown pressure. The same value of critical energy release rate is used for all conditions implying that G_c(35 N/m) does not have appreciable change with temperature which is in line with our molecular simulations (Wu and Firoozabadi 2022). The fracture patterns are shown in Fig. 5. A bi-wing fracture is observed at 20 °C without confinement (Fig. 5a, b),

and a few branches are observed under high temperature and confining pressure (Fig. 5c, d, f, g). Multiple small branches are more extensive at nonisothermal conditions (Fig. 5e, h) due to thermal effect; the pattern of created fractures is complex. In the experiments, some fractures are not initiated from the notch as shown in Fig. 5f which indicates that there are natural fractures in the granite used in experiment. Since the locations and the sizes of these natural fractures are not provided in Watanabe et al. (2017), we do not include them in our simulations. In future work, we will include the effect of natural fractures. As a whole, our simulated fracture patterns are in good agreement with experiments.

3.4 Hydraulic Fracturing by Water and by CO$_2$: Harcourt Granite

3.4.1 Hydraulic Fracturing by Water

Kumari et al. (2018) have conducted experiments on water fracturing in small cores of Harcourt granite. Water fracturing is investigated in unheated and heated Harcourt granite. The experiments are conducted without and with high boundary loading. The combination of loading and heated rocks provides data sets for the effect of thermoporoelasticity at high loading. The geometry is shown in Fig. 6a. The cylindrical sample is 22.5 mm diameter and length of 45 mm. The notch has a diameter of 3 mm. External loading is applied in the experiments by Kumari et al. (2018) with an axial stress of 65 MPa and 60 MPa confining pressure. Only confining pressure is accounted for in our 2D simulations. Insulation blanket is used to prevent heat loss. Closed boundary condition with no flow is applied for pressure, and insulation boundary condition is assumed for temperature in line with experimental setup. Granite specimens are fractured at room temperature of 20 °C, and at 300 °C; this will allow to investigate the effect of thermoporoelasticity.

Fig. 4 a Geometry of the setup and data from Watanabe et al. (2017); **b–d** pressure vs. time in the notch. Confining pressure = 40 MPa
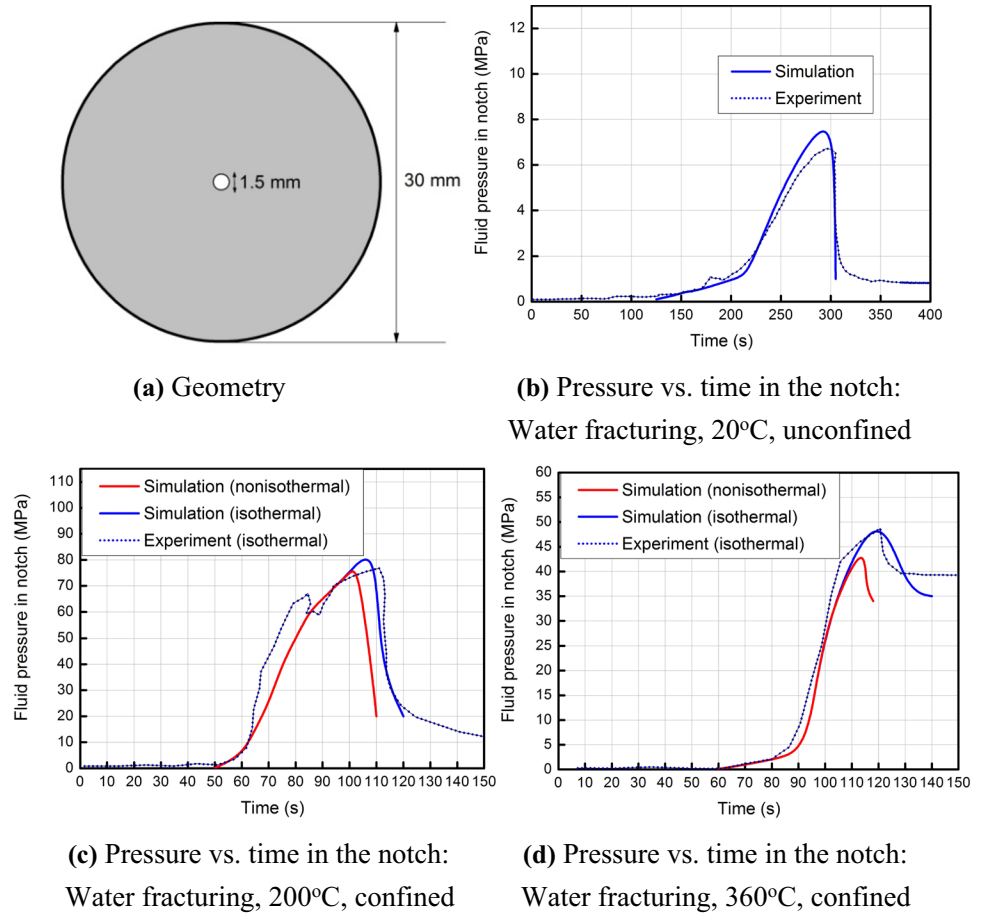

(a) Geometry

(b) Pressure vs. time in the notch: Water fracturing, 20°C, unconfined

(c) Pressure vs. time in the notch: Water fracturing, 200°C, confined

(d) Pressure vs. time in the notch: Water fracturing, 360°C, confined

Fig. 5 a–h Fracture pattern for water fracturing. **a**, **c**, **f** Adapted from Watanabe et al. (2017), with permission from Wiley. Confining pressure = 40 MPa
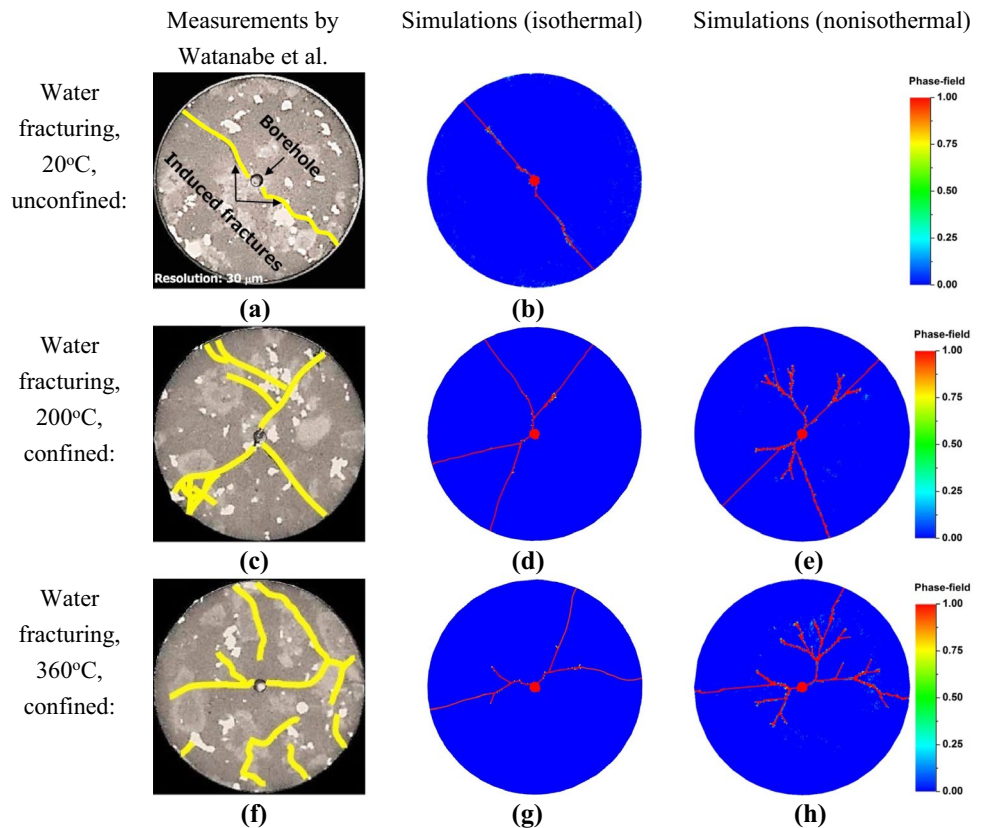
Table 3 Parameters used in simulation of experiments by Watanabe et al. (2017) (other parameters are the same as in Table 2)

ϕ	0.005	k_R	6.08×10^{-3} mD	α	0.005
Element size	0.1 mm	Q_p	5 mm²/s	G_c	35 N/m

The authors apply the high temperature and confining pressure for 3 h prior to fluid injection. Water fracturing is also conducted at 20 °C without confining pressure for comparison. We simulate the experiments in fracturing by water and conduct two additional simulations for fracturing by CO_2 at 50 and 300 °C. The temperature of fracturing fluids in the notch is kept at 20 °C for water and 50 °C for CO_2 in 2D. The relevant parameters of our simulations are listed in Table 4. Q_p in 2D is based on injection rate (5 mL/min) and length of hole (22 mm) from the experiments.

Figure 6b shows pressure vs. time in the notch. At room temperature, the breakdown pressure of water fracturing from simulations is 9.9 MPa without confinement and 72.0 MPa with confining pressure. The measured values are 9.3 MPa and 72.1 MPa, respectively. A much higher fluid pressure is needed to create tensile strain energy for fracture initiation at 60 MPa confining pressure. At 300 °C in hot

rock, the breakdown pressure is 68.0 MPa from simulation and 66.2 from experiment. The lower breakdown pressure is due to tensile thermal stress on cooled granite around the notch. The difference between measured and simulated breakdown pressure is less than 7% for the three conditions. We obtain the critical energy release rate $G_c = 100$ N/m by matching the breakdown pressure for the Harcourt granite-water systems; it does not change with temperature. The simulated breakdown pressure for CO_2 fracturing is about 65.6 MPa at 50 °C and 61.8 MPa at 300 °C. Fracturing of hot dry rock by CO_2 has lower breakdown pressure than by water, but the difference is not appreciable.

The fracture patterns are shown in Fig. 7. A bi-wing fracture is created for water fracturing without confinement (Fig. 7a, b), and multiple branches are observed under confining pressure (Fig. 7c-f). The fracture is more tortuous with more branches in hot dry rock (Fig. 7f). Our simulated fracture patterns are in good agreement with experimental data by Kumari et al. (2018). The CO_2-induced fracture has higher fracture surface area than water-induced fractures (Fig. 7g, h).

Fig. 6 **a** Geometry of the setup from Kumari et al. (2018); **b** pressure in the notch vs. time in water and CO_2 fracturing from simulations. Confining pressure = 60 MPa
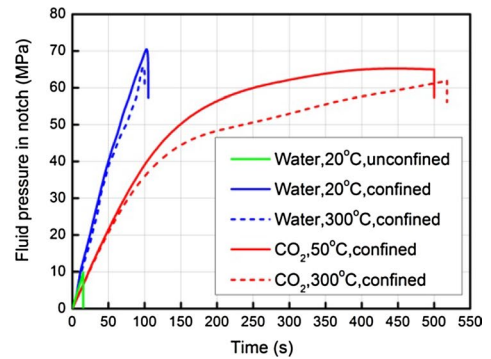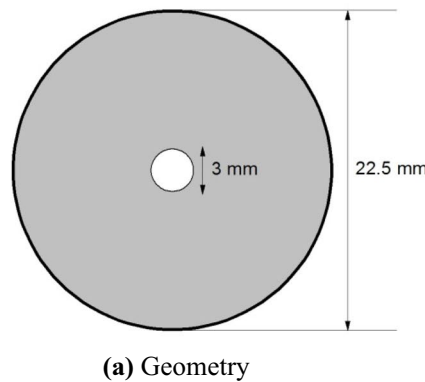
(a) Geometry

(b) Pressure vs. time in the notch: water and CO_2 fracturing in our simulations

Table 4 Parameters for simulation of Kumari et al. (2018) (G_c is obtained by matching the breakdown pressure)

E	1.82×10^{10} Pa	ν	0.22	$\alpha_{T,s}$	2.4×10^{-5} K^{-1}
$\alpha_{T,f}$	3×10^{-4} K^{-1} (water) 4×10^{-3} K^{-1} (CO_2)	$C_{V,s}$	790 J/(kg K)	ϕ	0.008
α	0.008	c_1	0.4	c_2	0.6
k_R	4.053×10^{-4} mD	l_0	0.25 mm	G_c	25 N/m (CO_2-Harcourt granite) 100 N/m (Water-Harcourt granite)
Element size	0.1 mm	Q_p	3.8 mm²/s	λ_s	3.1 W/(m K)

Fig. 7 **a–f** Fracture pattern for water fracturing; **g, h** fracture pattern for CO_2 fracturing. **a**, **c**, **e** are adapted from Kumari et al. (2018), with permission from Elsevier. Confining pressure = 60 MPa
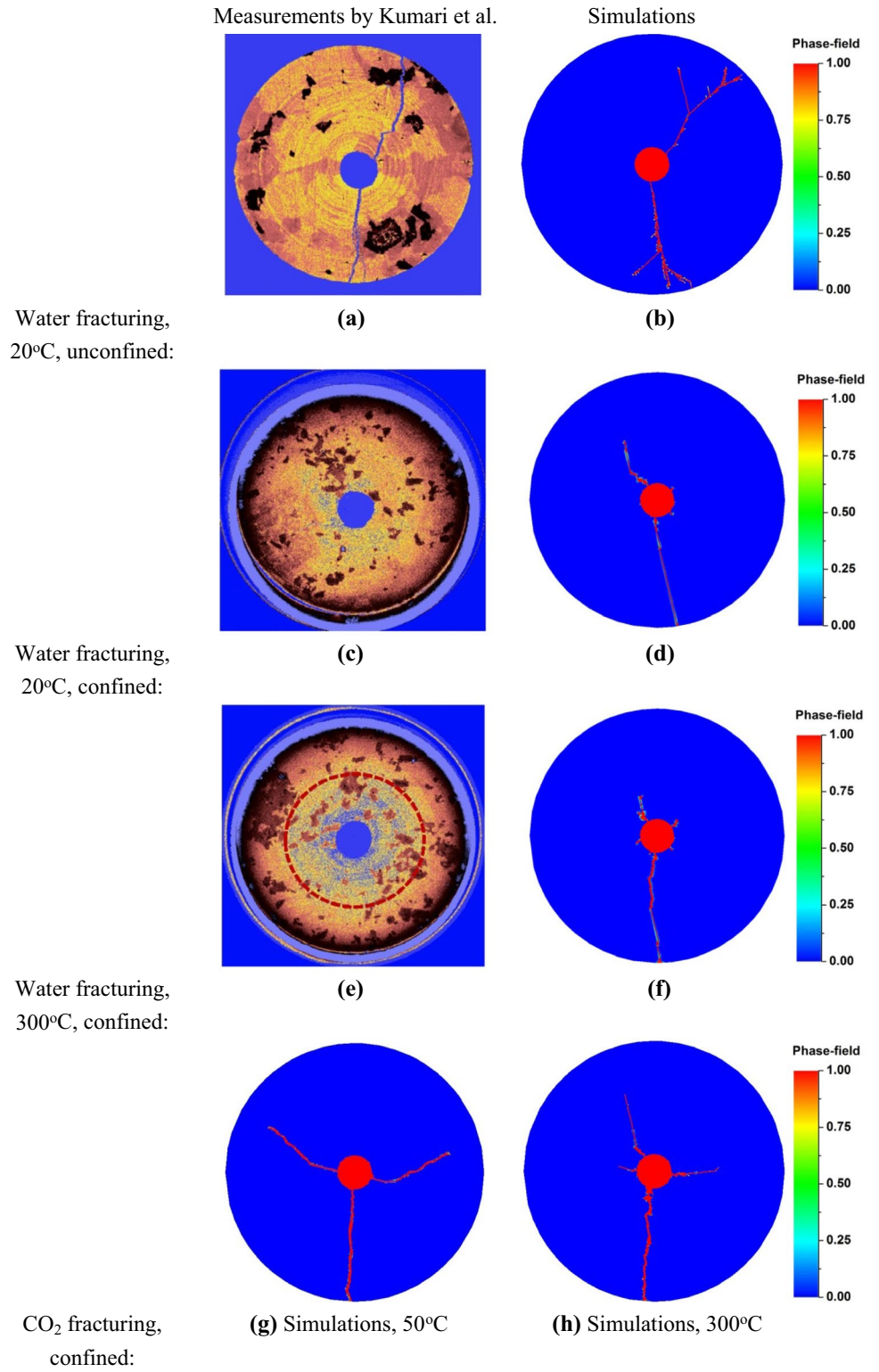

Measurements by Kumari et al.　　Simulations

Water fracturing, 20ºC, unconfined: 　　**(a)**　　**(b)**

Water fracturing, 20ºC, confined: 　　**(c)**　　**(d)**

Water fracturing, 300ºC, confined: 　　**(e)**　　**(f)**

CO_2 fracturing, confined: 　　**(g)** Simulations, 50ºC　　**(h)** Simulations, 300ºC

Table 5 Test conditions of Isaka et al. (2019) and breakdown pressure from experiment and simulation

Confining pressure (MPa)	Fracturing fluid	Temperature (°C)		Breakdown pressure (MPa)	
		Granite	Fluid	Experiment	Simulation
30	CO_2	50	40	42.6	43.3
		100	60	41.5	42.1
		200	80	39.3	39.5
		300	80	37.1	37.4
40	Water	20	20	Not reported	61.1
		100	20	Not reported	59.0
	CO_2	50	40	53.4	53.8
		100	60	52.3	52.5
		200	80	50.1	50.0
		300	80	47.9	47.8

3.4.2 Hydraulic Fracturing by CO_2

Isaka et al. (2019) have conducted experiments on CO_2 fracturing of small cores of Harcourt granite. The size of core is the same as Kumari et al. (2018) shown in Fig. 6a. An axial load with 5 MPa deviatoric stress is applied in the experiment but not in our simulations. E of Harcourt granite is 17 GPa. Q_p in 2D is 22.8 mm^2/s based on the injection rate (30 mL/min) from experiments. Other parameters of our simulations are the same as in Sect. 3.4.1 and are listed in Table 4. The conditions of confining pressure and temperature are summarized in Table 5. The experiments by Isaka et al. (2019) focus on CO_2 fracturing, and the breakdown pressure is not reported for water fracturing. From our simulations, fracturing of hot dry rock by CO_2 has lower breakdown pressure than water. In addition, the breakdown pressure is lower when confining pressure is lower or temperature is higher. The observation is consistent with the results presented in Sect. 3.4.1. Good agreement is found between experiments and simulations in all tests.

The CO_2-induced fracture patterns under 30 MPa confining pressure are shown in Fig. 8. A bi-wing fracture is observed below 100 °C (Fig. 8a–d), and multiple branches are observed at 200 and 300 °C (Fig. 8e–h).

The water-induced and CO_2-induced fracture patterns under 40 MPa confining pressure are shown in Figs. 9 and 10, respectively. A bi-wing fracture is observed for water fracturing (Fig. 9) and CO_2 fracturing at 50 °C (Fig. 10a, b) and 200 °C in the experiment (Fig. 10e). Three branches are observed for CO_2 fracturing at 100 °C (Fig. 10c, d), and multiple branches are observed at 300 °C (Fig. 10g, h). The CO_2-induced fracture has higher fracture surface area than water-induced fractures (Figs. 9, 10a–d). The fracture is more tortuous with more branches in hot dry rock (Fig. 10g,

h). Our simulated fracture patterns are in good agreement with experimental data by Isaka et al. (2019).

3.4.3 Hydraulic Fracturing by Water and by CO_2 in Larger Domain

In the simulations presented above, the fracture reaches the boundary within several milliseconds due to the small size of domain even when we stop injection after the breakdown pressure. In order to get insight into larger scale rock fracturing, we examine the fracture propagation in a five-time larger domain shown in Fig. 11a; the diameter is 112.5 mm. The size of notch and other conditions are kept the same as the smaller domain as listed in Table 4.

We first simulate fracturing by water. Figure 11b shows pressure vs. time in the notch. It takes 20 s for the pressure to reach the first breakdown point at a pressure of 13.73 MPa. The pressure drops significantly after breakdown to near zero, due to fluid filling of the created fractures. A bi-wing fracture is created as shown in Fig. 11c. Because of the large size of domain and low fluid pressure, the fracture stops propagating, and the second pressure buildup starts. The pressurization rate is lower than the condition before fracturing due to volume of created fractures, and the second breakdown pressure of 4.91 MPa is reached after 100 s. The following pressure buildups take longer with lower breakdown pressure as shown in Fig. 11b. Seven pressure buildup stages are observed before the fracture reaches the boundary of domain. The corresponding fracture pattern of each stage is shown in Fig. 11c–i. An example of pressure distribution during fourth pressure buildup is shown in Fig. 11j, k. At the beginning of pressure buildup, there is no fluid in new fractures (see Fig. 11j). It takes 150 s (from 270 to 420 s) to fill the new fractures. From 420 to 650 s, the fracture is filled

Fig. 8 Fracture pattern for CO_2 fracturing. **a**, **c**, **e**, **g** adapted from Isaka et al. (2019), with permission from Elsevier. Confining pressure = 30 MPa
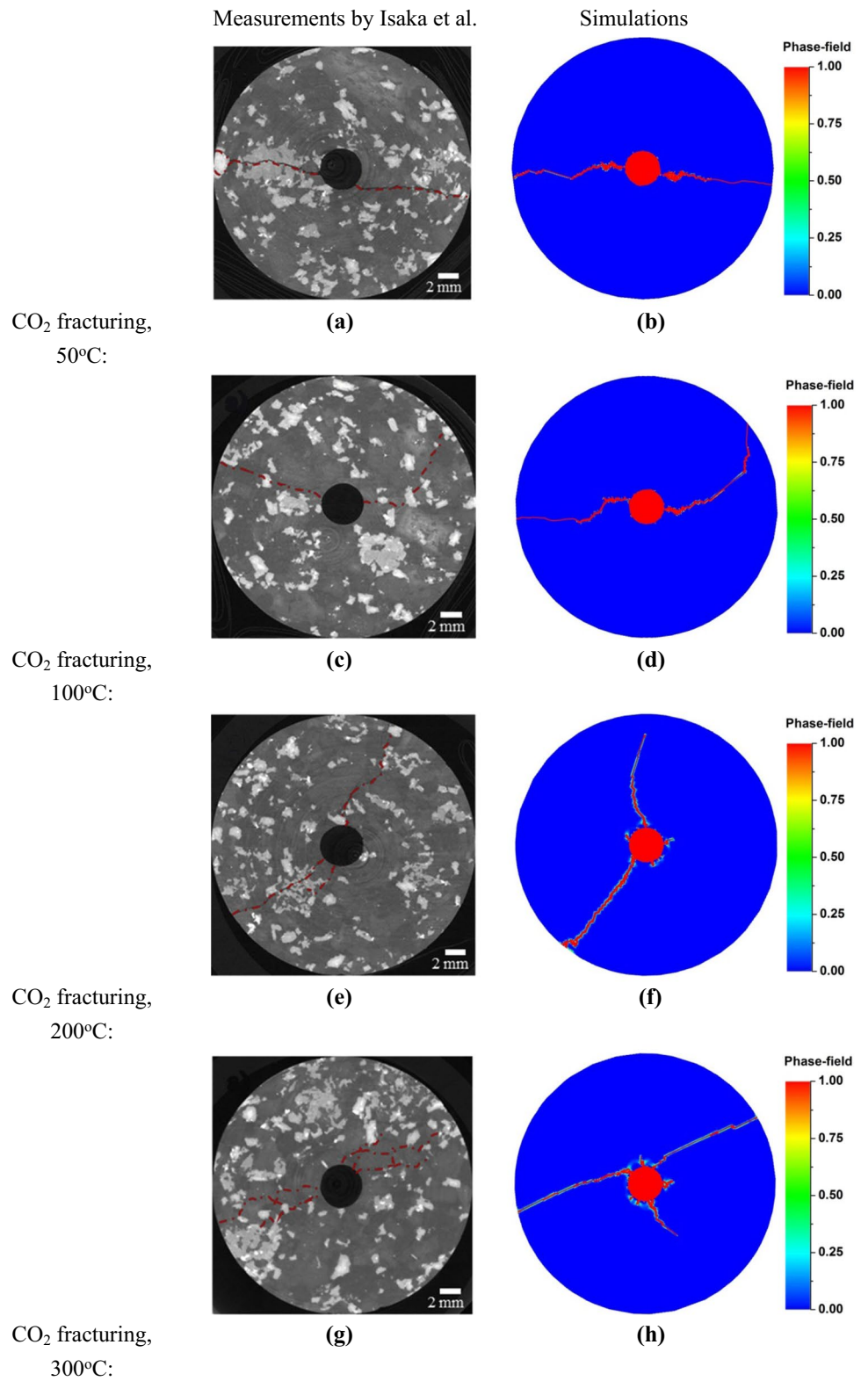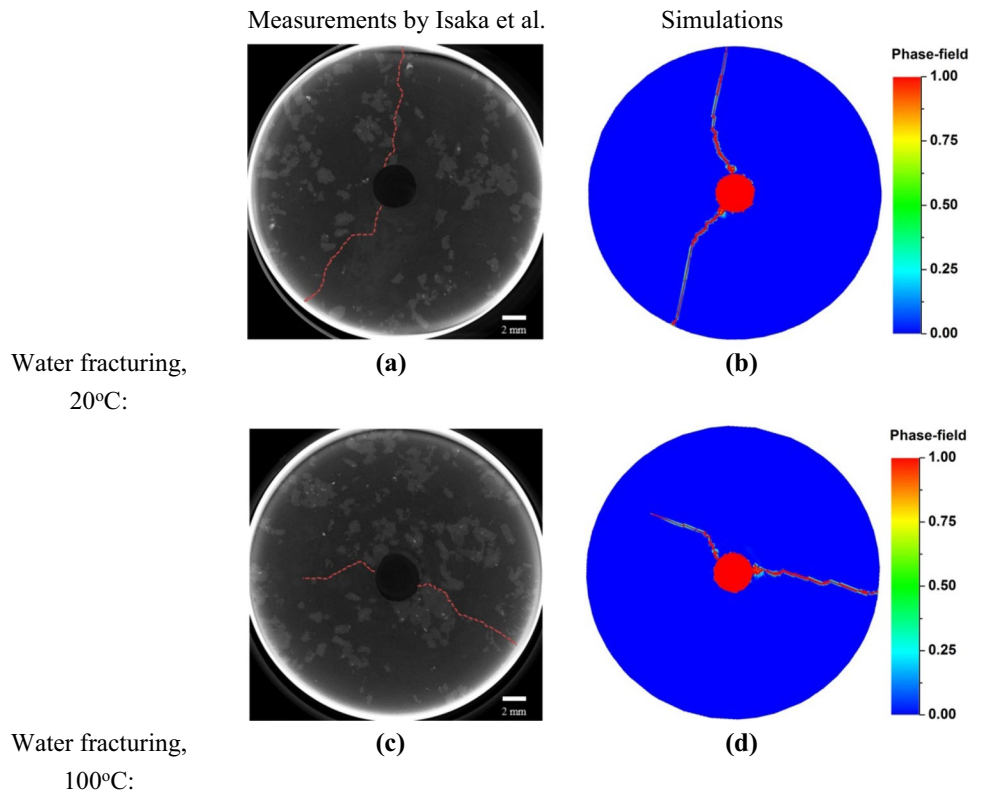
Fig. 9 Fracture pattern for water fracturing. **a**, **c** adapted from Isaka et al. (2019), with permission from Elsevier. Confining pressure = 40 MPa

Measurements by Isaka et al.   Simulations

Water fracturing, 20°C:

(a)   **(b)**

Water fracturing, 100°C:

(c)   **(d)**

with fluid, and the pressure increases to the breakdown point of 2.3 MPa as shown in Fig. 11k.

Figure 12 shows pressure distribution in the fracture before 5th pressure buildup from 700 to 1100 s. The fracture pattern corresponds to Fig. 11f. The pressure in the notch increases first as the fluid is injected, and the fracture is filled slowly as the fluid flows in. The pressurization rate in the notch increases significantly after 1100 s as the fracture pressure nearly reaches equilibrium.

We have also carried out simulations in the domain in Fig. 11a for CO_2 fracturing for both cold and hot dry rock. In addition, we have conducted water fracturing in hot dry rock. Figure 13a shows pressure vs. time in the notch for the two fluids at two temperatures without confinement. In water fracturing, the breakdown pressure drops from 13.7 to 12.7 MPa when the initial temperature of granite increases from 20 to 300 °C. For CO_2 fracturing, the breakdown pressure is about 9.5 MPa at 50 °C and 8.9 MPa at 300 °C. It takes longer for CO_2 to reach the breakdown pressure, but the pressure drop is much less than water during fracture propagation due to high CO_2 compressibility. There is only one short 2nd pressure buildup observed in CO_2 fracturing, and the fracture that propagates to the boundary is faster than water-induced fractures. The CO_2-induced fracture has branching, and a thermal damage zone is observed around the notch at high temperature (Fig. 13b–d).

We also examine water and CO_2 fracturing in a domain large than laboratory scale at high temperature at 60 MPa confining pressure. As shown in Fig. 14a, the breakdown pressure is 66.2 MPa for water and 64.6 MPa for CO_2. For both fluids, the pressure drops to near confining pressure after breakdown and decreases slowly during fracture propagation. A bi-wing fracture is observed for water fracturing (Fig. 14b), and multiple branches are observed for CO_2 fracturing (Fig. 14c).

4 Conclusions

We have advanced formulation of the phase field and numerical simulation of governing equations with consideration of thermoporoelasticity and full compressibility for CO_2. The simulation results of volcanic rocks are validated with laboratory experiments of water and CO_2 fracturing at nonisothermal conditions.

The following have been partly reported in the literature; we reconfirm them fully:

- The temperature of CO_2 due to expansion and compression may change in CO_2 fracturing even when the initial temperature of CO_2 and the rock are the same.
- Fracturing by water has higher breakdown pressure than by CO_2 in granite. The fractures induced by CO_2

Fig. 10 Fracture pattern for CO_2 fracturing. **a**, **c**, **e**, **g** adapted from Isaka et al. (2019), with permission from Elsevier. Confining pressure = 40 MPa
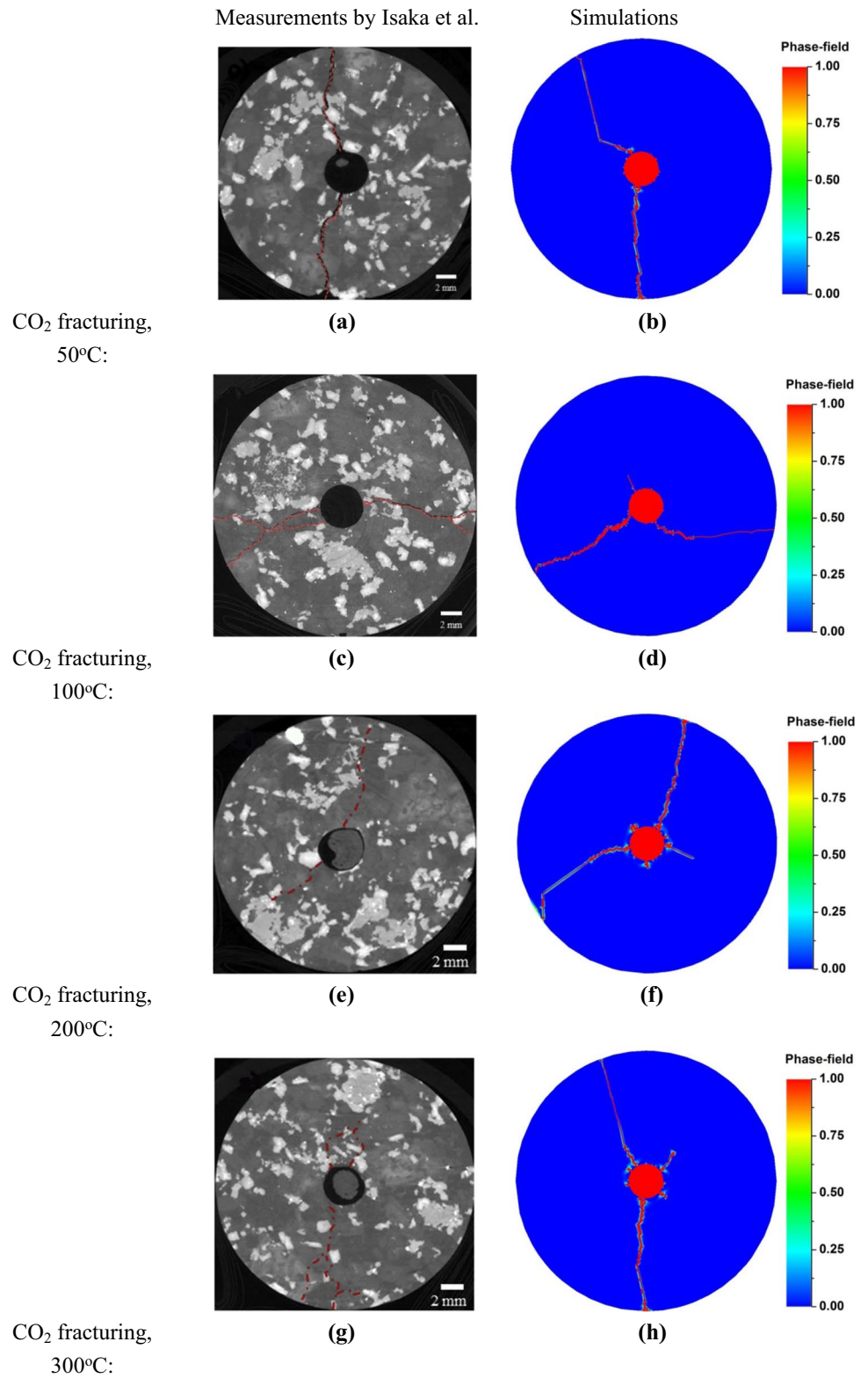
Fig. 11 **a** Geometry of the large domain simulation; **b** pressure in the notch vs. time in water fracturing; **c–i** phase-field profiles during fracture propagation; **j**, **k** pressure profiles during fracture propagation: unconfined domain. $T = 20$ °C
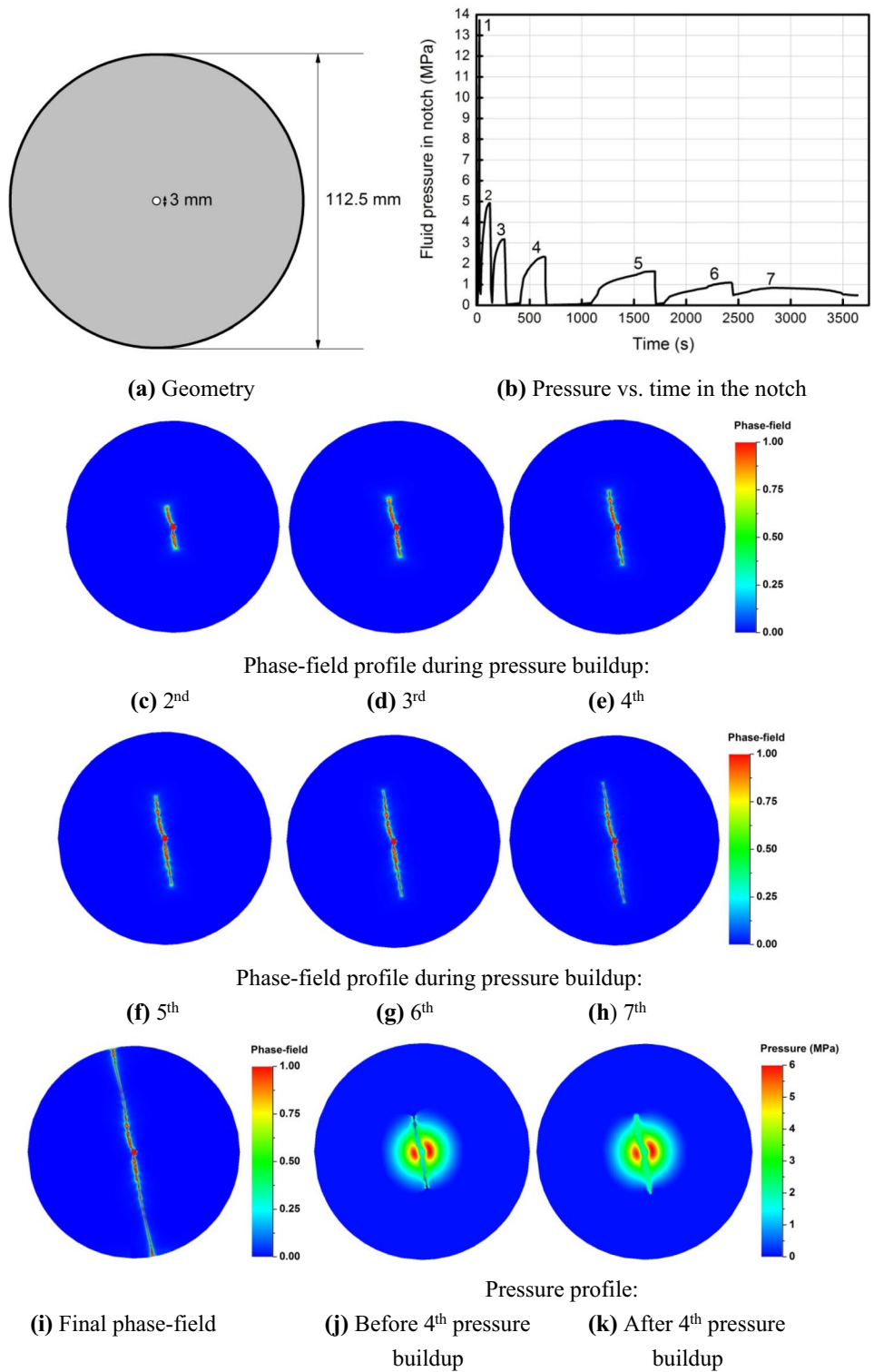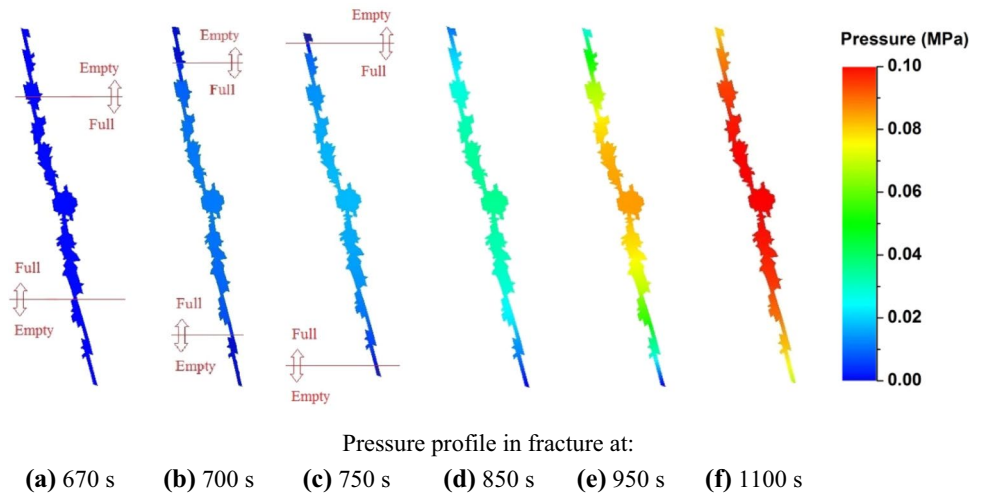

(a) Geometry

(b) Pressure vs. time in the notch

Phase-field profile during pressure buildup:

(c) 2nd **(d)** 3rd **(e)** 4th

Phase-field profile during pressure buildup:

(f) 5th **(g)** 6th **(h)** 7th

Pressure profile:

(i) Final phase-field   **(j)** Before 4th pressure buildup   **(k)** After 4th pressure buildup

Fig. 12 Pressure profiles in fracture before 5th buildup

Pressure profile in fracture at:

(a) 670 s **(b)** 700 s **(c)** 750 s **(d)** 850 s **(e)** 950 s **(f)** 1100 s

Fig. 13 **a** Pressure in the notch vs. time in water and CO_2 fracturing, large domain, unconfined condition; **b–d** phase-field profiles in water and CO_2 fracturing
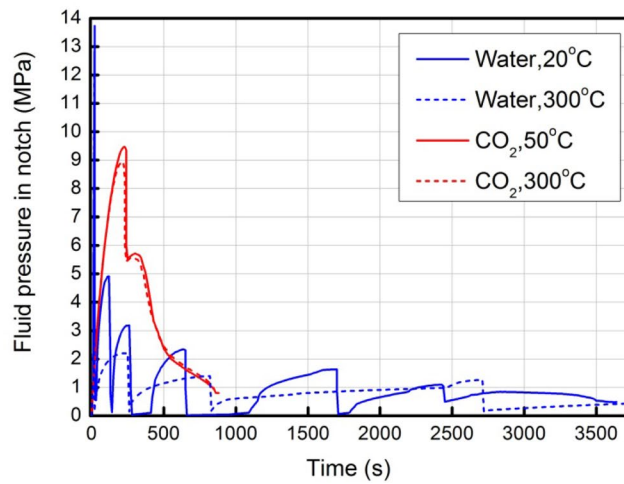
(a) Pressure vs. time in the notch

Final phase-field profile:

(b) water fracturing at 300ºC

(c) CO_2 fracturing at 50ºC

(d) CO_2 fracturing at 300ºC
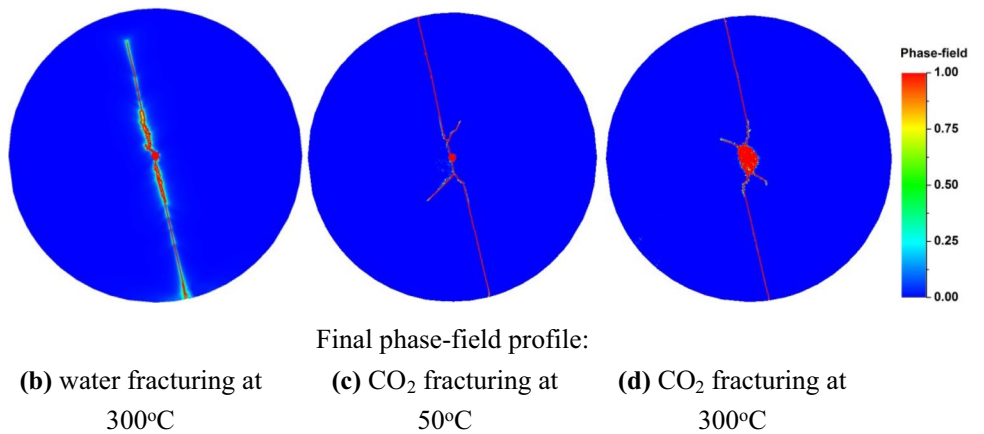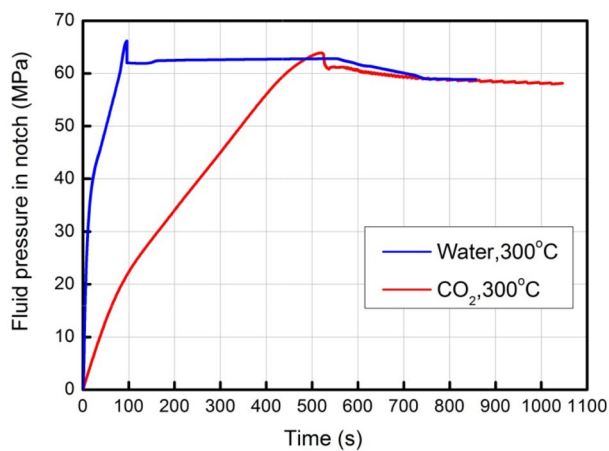
(a) Pressure vs. time in the notch
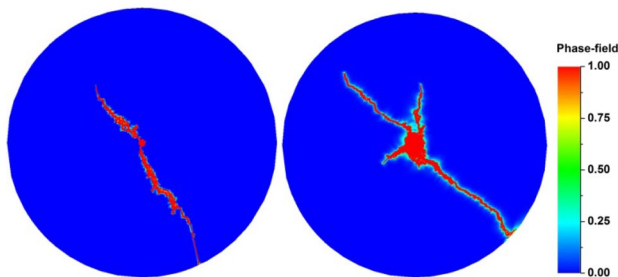
Final phase-field profile:

(b) water fracturing at 300°C | **(c)** CO_2 fracturing at 300°C

Fig. 14 **a** Pressure in the notch vs. time in water and CO_2 fracturing, large domain, confined condition; **b, c** phase-field profiles in water and CO_2 fracturing: confinement = 60 MPa

are more likely to have branching and complex patterns compared to water. The fracture surface area of CO_2 is higher than water.

- The critical energy release rate G_c of water–granite is higher than CO_2-granite. Higher G_c leads to higher breakdown pressure and lower G_c may lead to branching. The difference between G_c of CO_2-shale and water-shale may be higher than the corresponding G_c in granite.
- The breakdown pressure of granite at high temperature is lower than that of low-temperature granite. The reduction of breakdown pressure is much lower when there is confining pressure.

The new findings from our work are:

- We provide the critical energy release rate G_c of the water–granite. G_c is 35 N/m for Inada granite and 100 N/m for Harcourt granite. The critical energy release rate does not change appreciably with temperature. It is estimated to be 25 N/m for CO_2-granite.

- Fracturing beyond the small laboratory-scale experiments may have features different from laboratory scale. Because the fractures may propagate much faster than the fluids, there may be a significant difference between water fracturing and CO_2 fracturing in filling of created fractures. In water fracturing, the initial fractures created from the first breakdown pressure may stop until pressure buildup in the fracture reaches a second breakdown pressure and the process may be repeated. In CO_2 fracturing, due to CO_2 compressibility there may be continuous fracture propagation or less frequent stop and go.

The work has set the stage for advancing simulation of fracturing in 3D EGS systems and investigation of natural fractures on breakdown pressure and fracture propagation. The goal is to simulate fracturing in large-scale geothermal fields. The phase-field formulation advantage over alternative methods is that geometry of created fractures including branching can be predicted. In this work, we have used fine gridding in the whole domain because we do not know a priori where fractures will be created and do not have knowledge of where the propagation will lead to. An advanced dynamic adaptive gridding for fully compressible flow may be the key option.

Author contributions YF was involved in simulations, code development, and writing. AF was involved in conceptualization, funding acquire, and writing.

Declarations

Conflict of interest The authors, Yixuan Feng and Abbas Firoozabadi have no conflict of interest in relation to this work.

References

Al Shafloot T, Kim TW, Kovscek AR (2021) Investigating fracture propagation characteristics in shale using sc-CO_2 and water with the aid of X-ray computed tomography. J Nat Gas Sci Eng. https://doi.org/10.1016/j.jngse.2020.103736

Alpak FO (2021) A cohesive-zone model for simulating hydraulic-fracture evolution within a fully coupled flow/geomechanics-simulation system. SPE J 26(01):22–43. https://doi.org/10.2118/193825-PA

Bird RB, Stewart WE, Lightfoot EN (2002) Transport Phenomena. 2nd Edition, John Wiley & Sons Ltd., New York. http://dx.doi.org/10.1115/1.1424298

Bongole K, Sun Z, Yao J, Mehmood A, Yueying W, Mboje J, Xin Y (2019) Multifracture response to supercritical CO_2-EGS and water-EGS based on thermo-hydro-mechanical coupling method. Int J Energy Res. 43(13):7173–7196. https://doi.org/10.1002/er.4743

Borden MJ, Verhoosel CV, Scott MA, Hughes TJR, Landis CM (2012) A phase-field description of dynamic brittle fracture. Comput Methods Appl Mech Eng 217–220:77–95. https://doi.org/10.1016/j.cma.2012.01.008

Bourdin B, Francfort GA, Marigo JJ (2000) Numerical experiments in revisited brittle fracture. J Mech Phys Solids 48(4):797–826. https://doi.org/10.1016/S0022-5096(99)00028-9

Bourdin B, Marigo J-J, Maurini C, Sicsic P (2014) Morphogenesis and propagation of complex cracks induced by thermal shocks. Phys Rev Lett 112(1):014301. https://doi.org/10.1103/PhysRevLett.112.014301

Brown D (2000) A hot dry rock geothermal energy concept utilizing supercritical CO_2 instead of water. In: Proceedings of the twenty-fifth workshop on geothermal reservoir engineering

Castro CAND, Li SFY, Nagashima A, Trengove RD, Wakeham WA (1986) Standard reference data for the thermal conductivity of liquids. J Phys Chem Ref Data 15(3):1073–1086. https://doi.org/10.1063/1.555758

Chavent G, Roberts JE (1991) A unified physical presentation of mixed, mixed-hybrid finite elements and standard finite difference approximations for the determination of velocities in waterflow problems. Adv Water Resour 14(6):329–348. https://doi.org/10.1016/0309-1708(91)90020-O

Chen B, Barboza BR, Sun Y, Bai J, Thomas HR, Dutko M, Li C (2022) A review of hydraulic fracturing simulation. Arch Comput Methods Eng 29(4):1–58. https://doi.org/10.1007/s11831-021-09653-z

Chen B, Sun Y, Barboza BR, Barron AR, Li C (2020) Phase-field simulation of hydraulic fracturing with a revised fluid model and hybrid solver. Eng Fract Mech 229:106928. https://doi.org/10.1016/j.engfracmech.2020.106928

Chen B, Zhou Q (2021) Propagation, arrest, and reactivation of thermally driven fractures in an unconfined half-space using stability analysis. Theor Appl Fract Mech 114:102969. https://doi.org/10.1016/j.tafmec.2021.102969

Chen B, Zhou Q (2022) Scaling behavior of thermally driven fractures in deep low-permeability formations: a plane strain model with 1-D heat conduction. J Geophys Res Solid Earth 127(3):e2021JB022964. https://doi.org/10.1029/2021JB022964

Daneshy AA (1978) Hydraulic fracture propagation in layered formations. SPE J 18(01):33–41. https://doi.org/10.2118/6088-PA

Detournay E (2016) Mechanics of hydraulic fractures. Annu Rev Fluid Mech 48(1):311–339. https://doi.org/10.1146/annurev-fluid-010814-014736

Eckert ERGDRM (1987) Analysis of heat and mass transfer. Hemisphere Publishing Corp., Washington

Feng Y, Haugen K, Firoozabadi A (2021) Phase-field simulation of hydraulic fracturing by CO_2, water and nitrogen in 2D and comparison with laboratory data. J Geophys Res Solid Earth 126(11):e2021JB022509. https://doi.org/10.1029/2021JB022509

Francfort GA, Marigo JJ (1998) Revisiting brittle fracture as an energy minimization problem. J Mech Phys Solids 46(8):1319–1342. https://doi.org/10.1016/S0022-5096(98)00034-9

Gershenfeld N (1998) The nature of mathematical modeling. Cambridge University Press, Cambridge

Ghassemi A, Zhang Q (2004) A transient fictitious stress boundary element method for porothermoelastic media. Eng Anal Bound Elem 28(11):1363–1373. https://doi.org/10.1016/j.enganabound.2004.05.003

Ghassemi A, Zhou X (2011) A three-dimensional thermo-poroelastic model for fracture response to injection/extraction in enhanced geothermal systems. Geothermics 40(1):39–49. https://doi.org/10.1016/j.geothermics.2010.12.001

Griffith AA (1921) The phenomena of rupture and flow in solids. Philosophical Transactions A. 221:163 https://doi.org/10.1098/rsta.1921.0006

Guo T, Tang S, Liu S, Liu X, Zhang W, Qu G (2020) Numerical simulation of hydraulic fracturing of hot dry rock under thermal stress. Eng Fract Mech. https://doi.org/10.1016/j.engfracmech.2020.107350

Hoteit H., and Firoozabadi, A.: "Compositional Modeling by the Combined Discontinuous Galerkin and Mixed Methods," SPE Journal (March 2006) 19-34.

Inui S, Ishida T, Nagaya Y, Nara Y, Chen Y, Chen Q (2014) AE monitoring of hydraulic fracturing experiments in granite blocks using supercritical CO_2, water and viscous oil. In: Paper presented at the 48th U.S. rock mechanics/geomechanics symposium

Isaka B, Gamage R, Rathnaweera T, Perera M, Chandrasekharam D, Kumari W (2018) An influence of thermally-induced microcracking under cooling treatments: mechanical characteristics of australian granite. Energies. https://doi.org/10.3390/en11061338

Isaka BLA, Ranjith PG, Rathnaweera TD, Wanniarachchi WAM, Kumari WGP, Haque A (2019) Testing the frackability of granite using supercritical carbon dioxide: insights into geothermal energy systems. J CO_2 Util 34:180–197. https://doi.org/10.1016/j.jcou.2019.06.009

Ishida T, Aoyagi K, Niwa T, Chen Y, Murata S, Chen Q, Nakayama Y (2012) Acoustic emission monitoring of hydraulic fracturing laboratory experiment with supercritical and liquid CO_2. Geophys Res Lett. https://doi.org/10.1029/2012gl052788

Ishida T, Chen Q, Mizuta Y, Roegiers J-C (2004) Influence of fluid viscosity on the hydraulic fracturing mechanism. J Energy Res Technol 126(3):190–200. https://doi.org/10.1115/1.1791651

Kizaki A, Tanaka H, Ohashi K, Sakaguchi K, Matsuki K (2012) Hydraulic fracturing in Inada granite and Ogino tuff with super critical carbon dioxide. In: Paper presented at the ISRM regional symposium—7th Asian rock mechanics symposium

Kleiven S, Halldin P, Zenkert D (2001) Dynamic finite element methods—lecture notes for SD2450 biomechanics and neuronics

Kumari WGP, Ranjith PG, Perera MSA, Li X, Li LH, Chen BK, De Silva VRS (2018) Hydraulic fracturing under high temperature and pressure conditions with micro CT applications: geothermal energy from hot dry rocks. Fuel 230:138–154. https://doi.org/10.1016/j.fuel.2018.05.040

Lee S, Wheeler MF, Wick T (2016) Pressure and fluid-driven fracture propagation in porous media using an adaptive finite element phase field model. Comput Methods Appl Mech Eng 305:111–132. https://doi.org/10.1016/j.cma.2016.02.037

Li P, Li D, Wang Q, Zhou K (2021) Phase-field modeling of hydrothermally induced fracture in thermo-poroelastic media. Eng Fract Mech 254:107887. https://doi.org/10.1016/j.engfracmech.2021.107887

Li X, Cui L, Roegiers JC (1998) Thermoporoelastic modelling of wellbore stability in non-hydrostatic stress field. Int J Rock Mech Min Sci 35(4):584. https://doi.org/10.1016/S0148-9062(98)00079-5

Li X, Feng Z, Han G, Elsworth D, Marone C, Saffer D, Cheon D-S (2016) Breakdown pressure and fracture surface morphology of hydraulic fracturing in shale with H_2O, CO_2 and N_2. Geomech Geophys Geo-Energy Geo-Resour 2(2):63–76. https://doi.org/10.1007/s40948-016-0022-6

Li X, Li G, Yu W, Wang H, Sepehrnoori K, Chen Z, Zhang S (2018) Thermal effects of liquid/supercritical carbon dioxide arising from

fluid expansion in fracturing. SPE J 23(06):2026–2040. https://doi.org/10.2118/191357-pa

Lin W (2002) Permanent strain of thermal expansion and thermally induced microcracking in Inada granite. J Geophys Res Solid Earth 107(10):ECV 3-1-ECV 3-16. https://doi.org/10.1029/2001jb000648

Liu B, Suzuki A, Watanabe N, Ishibashi T, Sakaguchi K, Ito T (2022) Fracturing of granite rock with supercritical water for superhot geothermal resources. Renew Energy 184:56–67. https://doi.org/10.1016/j.renene.2021.11.062

Lohrenz J, Bray BG, Clark CR (1964) Calculating viscosities of reservoir fluids from their compositions. J Petrol Technol 16(10):1171–1176. https://doi.org/10.2118/915-PA

Miehe C, Hofacker M, Welschinger F (2010) A phase field model for rate-independent crack propagation: robust algorithmic implementation based on operator splits. Comput Methods Appl Mech Eng 199(45–48):2765–2778. https://doi.org/10.1016/j.cma.2010.04.011

Miehe C, Schänzel L-M, Ulmer H (2015) Phase field modeling of fracture in multi-physics problems. Part I. Balance of crack surface and failure criteria for brittle crack propagation in thermo-elastic solids. Comput Methods Appl Mech Eng 294:449–485. https://doi.org/10.1016/j.cma.2014.11.016

Noii N, Wick T (2019) A phase-field description for pressurized and non-isothermal propagating fractures. Comput Methods Appl Mech Eng 351:860–890. https://doi.org/10.1016/j.cma.2019.03.058

Peng D-Y, Robinson DB (1976) A new two-constant equation of state. Ind Eng Chem Fundam 15(1):59–64. https://doi.org/10.1021/i160057a011

Poling BE, Prausnitz JM, O'Connell JP (2001) The estimation of physical properties. In: Properties of gases and liquids, 5th edn. McGraw-Hill Education, New York

Pramudyo E, Goto R, Watanabe N, Sakaguchi K, Nakamura K, Komai T (2021) CO_2 injection-induced complex cloud-fracture networks in granite at conventional and superhot geothermal conditions. Geothermics. https://doi.org/10.1016/j.geothermics.2021.102265

Pruess K (2006) Enhanced geothermal systems (EGS) using CO_2 as working fluid—a novel approach for generating renewable energy with simultaneous sequestration of carbon. Geothermics 35(4):351–367. https://doi.org/10.1016/j.geothermics.2006.08.002

Rahbar H, Javanbakht M, Ziaei-Rad S, Reali A, Jafarzadeh H (2021) Finite element analysis of coupled phase-field and thermoelasticity equations at large strains for martensitic phase transformations based on implicit and explicit time discretization schemes. Mech Adv Mater Struct. https://doi.org/10.1080/15376494.2020.1870780

Reid RC (1975). Tables on the thermophysical properties of liquids and gases, 2nd edition. In: Vargaftik NB (ed), vol 21, no 6, pp 1235–1235. Halsted Press, New York https://doi.org/10.1002/aic.690210636

Salimzadeh S, Paluszny A, Zimmerman RW (2018) Effect of cold CO_2 injection on fracture apertures and growth. Int J Greenhouse Gas Control 74:130–141. https://doi.org/10.1016/j.ijggc.2018.04.013

Smejkal, T., Firoozabadi, A., & Mikyška, J. (2021). Unified thermodynamic stability analysis in fluids and elastic materials. *Fluid Phase Equilibria, 549*, 113219. doi:https://doi.org/10.1016/j.fluid.2021.113219

Sneddon IN, Lowengrub M (1969) Crack problems in the classical theory of elasticity. Wiley, New York

Stephens G, Voight B (1982) Hydraulic fracturing theory for conditions of thermal stress. Int J Rock Mech Min Sci Geomech Abstr 19(6):279–284. https://doi.org/10.1016/0148-9062(82)91364-X

Sun Y, Edwards MG, Chen B, Li C (2021) A state-of-the-art review of crack branching. Eng Fract Mech 257:108036. https://doi.org/10.1016/j.engfracmech.2021.108036

Tangella RG, Kumbhar P, Annabattula RK (2021) Hybrid phase-field modeling of thermo-elastic crack propagation. Int J Comput Methods Eng Sci Mech 23(1):29–44. https://doi.org/10.1080/15502287.2021.1904462

Tao Q, Ghassemi A (2010) Poro-thermoelastic borehole stress analysis for determination of the in situ stress and rock strength. Geothermics 39(3):250–259. https://doi.org/10.1016/j.geothermics.2010.06.004

Tarasovs S, Ghassemi A (2012) Radial cracking of a borehole by pressure and thermal shock. In: Paper presented at the 46th U.S. rock mechanics/geomechanics symposium

Watanabe N, Egawa M, Sakaguchi K, Ishibashi T, Tsuchiya N (2017) Hydraulic fracturing and permeability enhancement in granite from subcritical/brittle to supercritical/ductile conditions. Geophys Res Lett 44(11):5468–5475. https://doi.org/10.1002/2017GL073898

Wu T, Firoozabadi A (2021) Calculation of solid-fluid interfacial free energy with consideration of solid deformation by molecular dynamics simulations. J Phys Chem A 125(26):5841–5848. https://doi.org/10.1021/acs.jpca.1c00735

Wu T, Firoozabadi A (2022) Effect of fluids on the critical energy release rate of typical components in shale and andesite by molecular simulations. J Chem Phys 157(4):044701. https://doi.org/10.1063/5.0090157

Zhang W, Wang C, Guo T, He J, Zhang L, Chen S, Qu Z (2021) Study on the cracking mechanism of hydraulic and supercritical CO_2 fracturing in hot dry rock under thermal stress. Energy. https://doi.org/10.1016/j.energy.2021.119886

Zheng S, Li S, Zhang D (2021) Fluid and heat flow in enhanced geothermal systems considering fracture geometrical and topological complexities: an extended embedded discrete fracture model. Renew Energy 179:163–178. https://doi.org/10.1016/j.renene.2021.06.127

Zhou C, Wan Z, Zhang Y, Gu B (2018) Experimental study on hydraulic fracturing of granite under thermal shock. Geothermics 71:146–155. https://doi.org/10.1016/j.geothermics.2017.09.006

Zhou S, Zhuang X, Rabczuk T (2019) Phase-field modeling of fluid-driven dynamic cracking in porous media. Comput Methods Appl Mech Eng 350:169–198. https://doi.org/10.1016/j.cma.2019.03.001

Zidane A, Firoozabadi A (2014) An efficient numerical model for multicomponent compressible flow in fractured porous media. Adv Water Resour 74:127–147. https://doi.org/10.1016/j.advwatres.2014.08.010

Zienkiewicz OC (1982) Basic formulation of static and dynamic behaviours of soil and other porous media. Appl Math Mech 3(4):457–468. https://doi.org/10.1007/BF01908222